

<sup>1</sup>                   **Copyright**  
<sup>2</sup>                   **by**  
<sup>3</sup>                   **Ryan Patrick Hannigan**  
<sup>4</sup>                   **2023**

5 The Dissertation Committee for Ryan Patrick Hannigan certifies that  
6 this is the approved version of the following dissertation:

7 Stranger Things at the LHC

### **Committee:**

Christina Markert, Supervisor

Peter Onyisi

---

Aaron Zimmerman

---

Chandrajit Bajaj

8

9

**Stranger Things at the LHC**

10

by

11

**Ryan Patrick Hannigan, Ph.D.**

12

**Dissertation**

13

Presented to the Faculty of the Graduate School of

14

The University of Texas at Austin

15

in Partial Fulfillment

16

of the Requirements

17

for the degree of

18

**Doctor of Philosophy**

19

The University of Texas at Austin

20

May, 2023

To Jaynee.

## Chapter One: Introduction

23 The initial section of this chapter will mostly serve as a historical overview of the  
24 field of particle physics, leading to the development of the **Standard Model**: the  
25 theory that describes all of the fundamental<sup>1</sup> particles and the way in which they  
26 interact with each other. An emphasis will be made on the discovery of quarks and  
27 gluons, as the research presented in this thesis is centered around these particles.  
28 The second section will more thoroughly introduce the Standard Mode and its three  
29 distinct sectors, with the goal to provide a high-level mathematical overview of the  
30 theory.

31 The third section of this chapter will delve into the details of Quantum Chromo-  
32 Dynamics (QCD), which is the component of the Standard Model that describes the  
33 interactions between **quarks** and **gluons**, the constituent particles of the more famil-  
34 iar protons and neutrons. As many theoretical calculations are difficult to perform  
35 in QCD, the use of computationally-intensive numerical techniques is often required  
36 to make precise predictions. One such prediction is a phase transition from nuclear  
37 matter at everyday energies—in which the quarks and gluons are confined within  
38 protons and neutrons—into a novel state of matter at extreme temperatures or den-  
39 sities, known as the **Quark-Gluon Plasma** (QGP). Section ?? will detail the QGP  
40 and many of its interesting properties predicted by QCD, with an emphasis on the  
41 production of strange quarks within the plasma.

42 The final two sections of this chapter will discuss how high-energy particle col-  
43 lisions can be used to study the QGP, using both expensive particle accelerators  
44 (Section ??) and simulation techniques (Section ??).

---

<sup>1</sup>As of the year 2023, but reading this chapter will hopefully illustrate why this may be subject to change in the (likely very distant) future.

45 **1.1 What is fundamental?**

46 The answer to the question

47      What are the fundamental building blocks of our universe?

48 has changed drastically over the course of human history. The idea that all matter  
49 is composed of smaller, uncuttable pieces has been around since 5th century BCE  
50 when Greek philosophers Democritus and Leucippus first introduced the concept of  
51 an atom **GreekAtom**. While this idea was mostly motivated by philosophical rea-  
52 soning, it was later adopted by the English scientist John Dalton in the 19th century  
53 to explain the results of his chemical experiments, where he found that chemical  
54 elements always combined with each other by discrete units of mass **Dalton**. As  
55 scientists discovered more and more of these elements, the number of “fundamental”  
56 building blocks grew as well. By the late 1800s, over 70 unique chemical elements  
57 had been discovered, though they would often be grouped together due to similar  
58 chemical properties using what chemist Dimitri Mendeleev dubbed the *periodic ta-*  
59 *ble of elements* **PeriodicTable**. An example of the periodic table from the time of  
60 Mendeleev can be seen in Figure ???. While this grouping was useful for chemists,  
61 it also served as a hint to physicists that perhaps these elements were not actually  
62 fundamental, but rather composed of even smaller pieces.

63 Scientists’ understanding of the building blocks of matter changed again around  
64 the turn of the 20th century, with physicists J.J. Thomson, Ernest Rutherford, and  
65 James Chadwick determining that the supposedly indivisible atom was composed  
66 of even smaller subatomic particles, eventually named electrons, protons, and neu-  
67 trons **Electrons**, **Protons**, **Neutrons**. Thus the number of fundamental blocks of  
68 matter had decreased substantially from nearly 100 to just three. However, this  
69 number would need to be updated again only months later, as the fundamental  
70 anti-particle of the electron—known as the positron—was discovered in 1932 by  
71 Carl Anderson **Positron**. In the next two decades, the number of known funda-  
72 mental particles would skyrocket. In 1947, the muon was discovered **Muon**, fol-  
73 lowed by the discovery of a laundry list of particles **Kaon**, **Lambda**, **Sigma** that  
74 participate in the same interaction that holds the positively charged protons to-  
75 gether in the nucleus of an atom—the so-called **strong nuclear force**. These  
76 “fundamental” particles were collectively called **hadrons**, which were further sep-

		Ti = 50	Zr = 90	? = 180
		V = 51	Nb = 94	Ta = 182
		Cr = 52	Mo = 96	W = 186
		Mn = 55	Rh = 104,4	Pt = 197,4
		Fe = 56	Ru = 104,4	Ir = 198
H = 1	Ni =	Co = 59	Pd = 106,6	Os = 199
		Cu = 63,4	Ag = 108	Hg = 200
	Be = 9,4	Mg = 24	Zn = 65,2	Cd = 112
	B = 11	Al = 27,4	? = 68	Ur = 116
	C = 12	Si = 28	? = 70	Sn = 118
	N = 14	P = 31	As = 75	Sb = 122
	O = 16	S = 32	Se = 79,4	Te = 128?
	F = 19	Cl = 35,5	Br = 80	J = 127
Li = 7	Na = 23	K = 39	Rb = 86,4	Cs = 133
		Ca = 40	Sr = 87,6	Ba = 137
		? = 45	Ce = 92	Tl = 204
		?Er = 56	La = 94	Pb = 207
		?Yt = 60	Di = 95	
		?In = 75,6	Th = 118?	

Figure 1.1: Dimitri Mendeleev’s periodic table of elements from the late 1800s, taken from [MendeleevPaper](#). The elements are grouped by similar chemical properties, and the gaps in the table are where Mendeleev predicted that new elements would be discovered.

77 arated into lighter and heavier categories, dubbed **mesons** and **baryons**, respec-  
 78 tively **MesonBaryon**. By the late 1960s, the number of known hadrons had grown  
 79 to well over 100 **ParticleDiscoveries**, even more than the number of “fundamental”  
 80 chemical elements that were known to exist in the 1800s.

81 In the same way that Mendeleev tried to group the elements by their similar  
 82 chemical properties, physicists attempted to group the hadrons together based on  
 83 their known subatomic properties. The first successful attempt at such a grouping was  
 84 the **Eightfold Way**, which was independently proposed by Murray Gell-Mann and  
 85 Yuval Ne’eman in 1961 **GellMannEightfold**, **NeemanEightfold**. This grouping  
 86 was found by examining the following properties of the hadrons:

- 87 1. **Isotopic spin**: a quantum number introduced by Werner Heisenberg in 1932  
 88 to try to explain the apparent symmetries between the proton and neutron with  
 89 respect to the strong nuclear force **IsotopicSpin** (i.e. although the proton and  
 90 neutron have different electric charges, the strong interaction does not seem to  
 91 distinguish between the two)
- 92 2. **Strangeness**: another quantum number introduced by Gell-Mann and Nishi-  
 93 jima in 1953 to explain why some hadrons decayed much more slowly than  
 94 expected, and such particles appeared to be created in pairs **Strangeness**. In

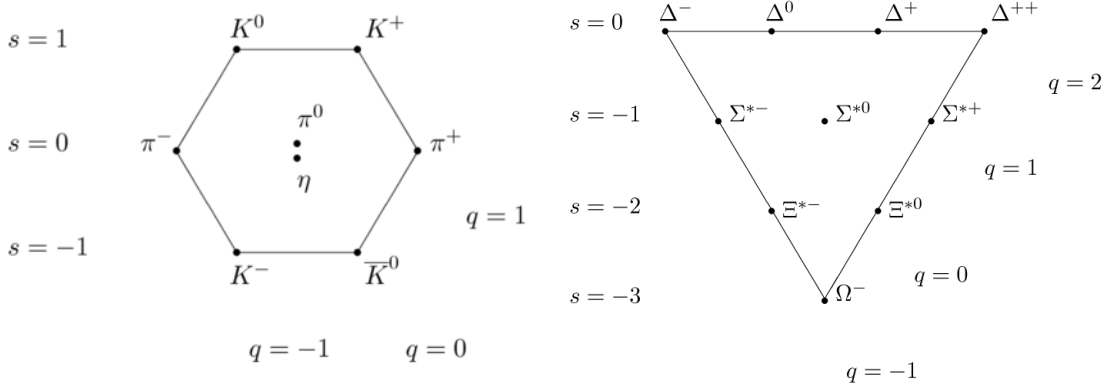


Figure 1.2: The “Eightfold Way” diagrams of the  $J = 1/2$  mesons (left) and  $J = 3/2$  baryons (right) plotted against strangeness and electric charge. Understanding the underlying symmetry group that gives rise to such patterns<sup>3</sup> ultimately led to the development of the quark model. While the original patterns were found using isotopic spin and hypercharge, it is trivial to convert between the two using the Gell-Mann-Nishijima formula [GellMannNishijima`1](#), [GellMannNishijima`2](#).

other words, the strong interaction responsible for the creation of these particles appeared to conserve this quantum number, but the weak interaction responsible for the slower decay of these particles did not. Strangeness<sup>2</sup> will be discussed in more detail in Section ??.

Plotting the baryons and mesons in a two-dimensional space based on these two properties revealed striking patterns, as shown in Figure ???. Similar to Mendeleev, GellMann also left a blank space<sup>4</sup> where he believed a new particle—the  $\Omega^-$ —would be discovered. The patterns in these diagrams hinted at an underlying symmetry governing the strong nuclear force, and ultimately led to the invention of the very first quark model by Gell-Mann and Zweig in 1964 **QuarkModel**. This model proposed that all of the hadrons were actually composed of even smaller particles, which Gell-Mann dubbed “quarks”. The quark model was able to explain the patterns seen

---

<sup>2</sup>The “strangeness” being referred to in this section was introduced a few years before the very first quark model, but it now has the modern interpretation which is directly related to the number of strange and anti-strange quarks within a hadron.

<sup>3</sup>Namely  $SU(3)$ , but this is a history lesson. Also the path from  $SU(3)$  to patterns of this type is long and arduous, involving a thorough understanding of representation theory.

<sup>4</sup>The original paper on the Eightfold Way does not contain any of these diagrams, but there are discussions about the properties of particles that should exist if the theory were correct, but had not been observed **GellMannEightfold**.

107 in Figure ?? by introducing three different types of fermionic quarks—up, down and  
108 strange—along with their corresponding anti-quarks. Baryons would then be composed  
109 of three such quarks, whereas mesons would be composed of quark and anti-quark  
110 pairs. If the quark model were correct, the number of fundamental building blocks  
111 of matter would again decrease from over 100 to just 14: electrons, muons, electron  
112 neutrinos, muon neutrinos, up quarks, down quarks, strange quarks, and all of their  
113 corresponding anti-particles.

114 Initially, many physicists believed that the quarks from this model were just a  
115 mathematical abstraction **QuarkAbstraction**. This possibility did not stop Shel-  
116 don Glashow and James Bjorken from extending the quark model less than a year  
117 after its inception by introducing a fourth quark: the charm **CharmQuark**. This  
118 new quark was primarily introduced to equalize the number of leptons (four at the  
119 time: electron, muon, and their respective neutrinos) with the number of quarks.  
120 The theory was mostly aesthetic **AestheticCharm** in that the charm quark was  
121 not explicitly required by any known mechanisms. It was only after the Glashow-  
122 Iliopoulos-Maiani (GIM) mechanism was introduced in 1970 **GIM** that the existence  
123 of the charm quark became necessary. This mechanism helped explain why neutral  
124 kaons decayed into two muons at a much lower rate than expected, but it required  
125 the existence of a quark with the same charge as the up quark but with a much larger  
126 mass.

127 The notion that protons and neutrons were fundamental particles was also being  
128 challenged on the experimental side. The deep inelastic scattering experiments at  
129 the Stanford Linear Accelerator Center (SLAC) performed by Kendall, Friedman,  
130 and Taylor in 1968 **Kendall, Friedman, Taylor** revealed unexpected<sup>5</sup> behavior  
131 when probing the structure of the proton: it appeared to be composed of point-  
132 like particles. These experiments were performed by firing electrons at stationary  
133 protons and measuring the energy distributions of the scattered electrons at different  
134 scattering angles. An example of such a distribution for electrons with initial energies  
135 of 10 GeV scattered at 6 degrees can be seen in Figure ???. The large spike on  
136 the left side of the distribution corresponds to the elastic scattering of the electron  
137 off the proton, which was well understood at the time **ElasticScattering**. The  
138 “bumps” observed at lower values of the scattered electron energy were also well

---

<sup>5</sup>Depending on who you asked at the time, both the three and four quark models were not universally accepted.

understood **Resonances**, and they correspond to the “shallow” inelastic scattering of the electron off the proton, where the proton gets excited into a so-called *resonance* state (like the  $\Delta$  baryon). However, the “background” underneath the bumps and the apparent continuum of events at even lower values of the scattered electron energy corresponded to a host of unknown particles being produced. This host of particles appeared to grow with increasing scattering angle and decreasing scattered electron energy, which ultimately led to the conclusion that the proton was composed of point-like particles that were being “knocked out” of the proton by the incoming electron **Kendall, BjorkenScaling**.

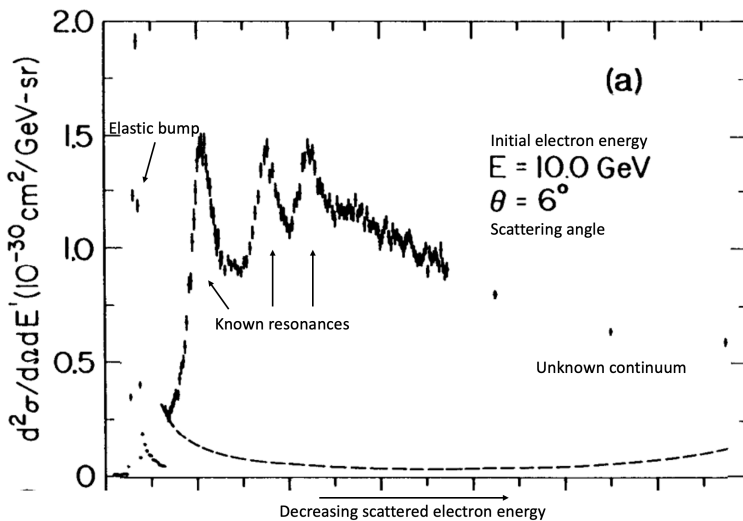


Figure 1.3: The energy distribution of electrons scattered off of protons at an initial electron energy of 10 GeV and a scattering angle of 6 degrees. The large spike on the left side of the distribution corresponds to the elastic scattering of the electron off the proton, and the “bumps” correspond to the inelastic scattering of the electron off the proton. The “background” underneath the bumps and the apparent continuum of events at even lower values of the scattered electron energy correspond to a mess of unknown particles being produced. The behavior of this continuum with respect to the scattering angle and the scattered electron energy ultimately led to the conclusion that the proton was not fundamental.

While many physicists were perfectly happy to interpret these point-like particles as the very same quarks from the aforementioned quark model(s), they received the much more noncommittal name **partons** after Richard Feynman’s parton model of hadrons **Partons**. The association of these partons with quarks was not universally

152 accepted<sup>6</sup> until the discovery of the  $J/\psi$  meson in 1974 **Jpsi**. In the meantime, the  
153 theoretical description of the strong nuclear force was closing in on its final form. The  
154 formulation of Quantum ChromoDynamics (QCD) in the early 1970s by Gell-Mann,  
155 Fritzsch, and Leutwyler **QCDFormulation** resolved many of the issues that were  
156 present in the initial quark models<sup>7</sup>. QCD introduced the concept of color charge,  
157 which all of the quarks would carry. The mediating bosons of the strong interaction—  
158 known as **gluons**—were also introduced, carrying color charge as well.

159 While QCD gave a solid mathematical description of the strong interaction, it  
160 wasn't until the discovery of **asymptotic freedom** **AssFreedom1**, **AssFreedom2**  
161 by Gross, Wilczek, and Politzer in 1973 that the theory became experimentally  
162 testable. Asymptotic freedom refers to the property that the strong interaction be-  
163 comes weaker at higher energies, allowing for QCD calculations to be performed using  
164 perturbative techniques. This discovery allowed theorists to use QCD to make predi-  
165 tions of the results of very high energy particle collision experiments. The first QCD  
166 prediction to be experimentally verified came from the Positron-Electron Tandem  
167 Ring Accelerator (PETRA) in 1979 **PETRA**, which experimentally confirmed the  
168 existence of gluons **GluonConfirmation**. With experimental verification of QCD, it  
169 became clear that the association of partons with quarks was indeed incorrect: they  
170 are both quarks *and* gluons.

171 In addition to the theory of QCD, the theory of electroweak interactions was also  
172 being developed during the 1960s by Glashow, Weinberg, and Salam **Electroweak1**,  
173 **Electroweak2**. With this new theory came the prediction of four<sup>8</sup> new bosons: the  
174 Higgs boson, the charged  $W^\pm$  bosons, and the neutral  $Z^0$  boson. With the combined  
175 theories of the electroweak and strong interaction, the **Standard Model** of particle  
176 physics—which describes the now 61<sup>9</sup> fundamental particles and how they interact—  
177 was complete.

---

<sup>6</sup>No acceptance of any model is a step function, but the discovery of  $J/\psi$  seems to be a turning point in literature.

<sup>7</sup>For example, the wavefunction of the  $\Delta^{++}$  baryon under the first quark model was not anti-symmetric, which is a requirement for fermions.

<sup>8</sup>The Higgs mechanism (which predicts the existence of the Higgs boson) came before electroweak unification **HiggsPaper**, but it was a requirement for the theory.

<sup>9</sup>There are many ways to count fundamental particles, but this particular number is obtained by: 6 leptons ( $\times 2$  for anti-leptons), 6 quarks ( $\times 3$  for each color,  $\times 2$  for anti-quarks), 1 gluon ( $\times 8$  for color), 1 photon, the  $W$  and  $Z$  bosons, and the Higgs boson.

<sup>178</sup> **1.2 The Standard Model**

<sup>179</sup> The Standard Model of particle physics is a **quantum field theory** (QFT) that  
<sup>180</sup> describes the interactions between all<sup>10</sup> of the fundamental particles. QFTs describe  
<sup>181</sup> the dynamics of a quantum system in terms of fields, which are functions of space and  
<sup>182</sup> time. The fields are the fundamental objects of QFT, and their excitations correspond  
<sup>183</sup> to the particles that are observed in nature. The Standard Model fields can be broken  
<sup>184</sup> down into three sectors, which will be discussed in the following sections.

<sup>185</sup> **1.2.1 The gauge sector**

<sup>186</sup> The gauge sector of the Standard Model corresponds to the spin-one bosons that  
<sup>187</sup> mediate the strong and electroweak interactions. In a general sense, this sector corre-  
<sup>188</sup> sponds to the mediating particles for three of the four fundamental forces: the strong  
<sup>189</sup> nuclear force, the weak nuclear force, and the electromagnetic force. The fourth  
<sup>190</sup> fundamental force—gravity—is not included in the Standard Model, as it is not yet  
<sup>191</sup> understood from a quantum perspective **QuantumGravity**.

<sup>192</sup> The symmetry group of the gauge sector is given by

$$\text{SU}(3)_c \times [\text{SU}(2)_L \times \text{U}(1)_Y]. \quad (1.1)$$

<sup>193</sup>  $\text{SU}(3)_c$  is the symmetry group of the strong interaction, which is described by the QFT  
<sup>194</sup> known as Quantum ChromoDynamics (QCD). The subscript  $c$  stands for “color”,  
<sup>195</sup> indicating that the gauge fields in QCD (gluons) only couple to colored objects.  
<sup>196</sup> QCD will be discussed in more detail in Section ???. The symmetry group of the  
<sup>197</sup> electroweak interaction is  $\text{SU}(2)_L \times \text{U}(1)_Y$ , where the subscript  $L$  stands for “left-  
<sup>198</sup> handed” and the subscript  $Y$  stands for “weak hypercharge”. Again, these subscripts  
<sup>199</sup> indicate the types of objects to which the corresponding gauge fields couple. For  
<sup>200</sup> example, the gauge fields of  $\text{SU}(2)_L$  only couple to left-handed objects, and the gauge  
<sup>201</sup> fields of  $\text{U}(1)_Y$  only couple to weakly hypercharged objects. Initially, there are four  
<sup>202</sup> massless gauge fields in the electroweak theory<sup>11</sup>. After the spontaneous symmetry  
<sup>203</sup> breaking of the Higgs mechanism **HiggsPaper**, these fields mix to give rise to three  
<sup>204</sup> massive gauge fields and one massless gauge field. The three massive gauge fields

---

<sup>10</sup>Ignoring potential gravitons **Graviton** or dark matter candidates **DarkMatter1**

<sup>11</sup>Three corresponding to the generators of  $\text{SU}(2)$ , one corresponding to the generator of  $\text{U}(1)$ .

205 correspond to the familiar  $W^\pm$  and  $Z^0$  bosons, which are the mediating bosons of  
206 the weak interaction. The massless gauge field corresponds to the photon, which  
207 mediates the electromagnetic interaction.

### 208 1.2.2 The scalar sector

209 The scalar sector of the Standard Model is quite lonely, and only corresponds to one  
210 spin-zero field: the Higgs **HiggsPaper**. As mentioned in the previous section, the  
211 Higgs mechanism that corresponds to this field is responsible for the acquisition of  
212 mass by the  $W^\pm$  and  $Z^0$  bosons. The Higgs field also couples to all of the fermions in  
213 the Standard Model, but the mass acquisition procedure is *slightly* different<sup>12</sup> from  
214 the massive bosons. The associated Higgs boson was discovered by the A Toroidal  
215 LHC Apparatus (ATLAS) and Compact Muon Solenoid (CMS) collaborations in  
216 2012 **HiggsDiscovery1**, **HiggsDiscovery2**, and was the last major piece of the  
217 Standard Model to be experimentally verified.

### 218 1.2.3 The fermionic sector

219 The fermionic sector contains all of the spin one-half particles (quarks and leptons) in  
220 the Standard Model. It is often convenient to group these particles into three genera-  
221 tions, where each generation is identical except for the masses of the particles. It is  
222 even *more* convenient to group the fermions within each family into multiplets, where  
223 the members of the multiplet are related to each other by transformations within the  
224 gauge group of the Standard Model (Equation ??). In other words, the fermions  
225 within a particular multiplet can only be transformed to fermions within the same  
226 multiplet. A table of the fermions in the Standard Model and their corresponding  
227 multiplets can be seen in Table ???. The indices  $L$  and  $R$  correspond to the chirality  
228 of the fields, and the indices  $r$ ,  $g$ , and  $b$  represent the color charge of the fields. The  
229 color charges are only non-zero for the quarks, making them the only fermions that  
230 couple to the gauge fields of the strong interaction (gluons).

---

<sup>12</sup>It's still spontaneous symmetry breaking, but within the Yukawa part of the electroweak La-  
grangian.

Table 1.1: The fermions of the Standard Model for each generation and their corresponding multiplets. The Standard Model does not allow for fermions to leave their respective multiplets.

Gen.	Left-handed quarks	Right-handed up quarks	Right-handed down quarks	Left- handed leptons	Right- handed leptons
1 <sup>st</sup> gen.	$\begin{pmatrix} u_L^r & u_L^g & u_L^b \\ d_L^r & d_L^g & d_L^b \end{pmatrix}$	$(u_R^r \ u_R^g \ u_R^b)$	$(d_R^r \ d_R^g \ d_R^b)$	$\begin{pmatrix} \nu_{eL} \\ e_L \end{pmatrix}$	$(e_R)$
2 <sup>nd</sup> gen.	$\begin{pmatrix} c_L^r & c_L^g & c_L^b \\ s_L^r & s_L^g & s_L^b \end{pmatrix}$	$(c_R^r \ c_R^g \ c_R^b)$	$(s_R^r \ s_R^g \ s_R^b)$	$\begin{pmatrix} \nu_{\mu L} \\ \mu_L \end{pmatrix}$	$(\mu_R)$
3 <sup>rd</sup> gen.	$\begin{pmatrix} t_L^r & t_L^g & t_L^b \\ b_L^r & b_L^g & b_L^b \end{pmatrix}$	$(t_R^r \ t_R^g \ t_R^b)$	$(b_R^r \ b_R^g \ b_R^b)$	$\begin{pmatrix} \nu_{\tau L} \\ \tau_L \end{pmatrix}$	$(\tau_R)$

## 231 1.3 Quantum chromodynamics

232 Quantum chromodynamics (QCD) is the component of the Standard Model that  
 233 describes the strong interaction between quarks and gluons, the fundamental particles  
 234 that make up most of the matter in the universe. In this theory, the fermionic quarks  
 235 have “color charge”, which can either be red, green or blue for quarks, or anti-red,  
 236 anti-green, or anti-blue for anti-quarks. The gluons, which are the mediating bosons  
 237 of the strong interaction, also carry color charge, but in the form of a superposition of  
 238 both color and anti-color. This section will delve into the details of QCD, emphasizing  
 239 the properties of the strong interaction that make it so challenging to study.

### 240 1.3.1 The QCD Lagrangian

The dynamics of the Standard Model fields and how they interact are completely encoded within the Lagrangian of the theory, which can be used to calculate experimental observables like cross-sections and decay rates. However, the Lagrangian of the Standard Model is fairly long **StandardModelLength1**, and often not particularly insightful when trying to study a specific aspect of the theory. As such, when studying QCD, it is often useful to throw away the electroweak gauge fields, leptons, and scalars to look at only the QCD Lagrangian **QCDHistory**,

$$\begin{aligned} \mathcal{L}_{QCD} = & -\frac{1}{4} F_{\mu\nu}^A F^{A\mu\nu} + i\bar{q}\gamma^\mu \left( \partial_\mu + ig_s \frac{1}{2} \lambda^A \mathcal{A}_\mu^A \right) q \\ & - \bar{q}_R \mathcal{M} q_L - \bar{q}_L \mathcal{M}^\dagger q_R - \theta\omega, \end{aligned}$$

241 where all repeated indices are summed over.

242 The gluons are described by the vector gauge field  $\mathcal{A}_\mu^A$ , with index  $A$  representing  
243 one of the eight color labels. These eight components belong to the color group  
244  $SU_c(3)$ , which is the gauge group of QCD. The corresponding coupling constant is  
245  $g_s$ , and the field strength tensor  $F_{\mu\nu}^A$  is given by

$$F_{\mu\nu}^A = \partial_\mu \mathcal{A}_\nu^A - \partial_\nu \mathcal{A}_\mu^A + g_s f^{ABC} \mathcal{A}_\mu^B \mathcal{A}_\nu^C, \quad (1.2)$$

246 where  $f^{ABC}$  are the structure constants **StructureConstants** of  $SU_c(3)$ . Note that  
247 while this field strength tensor shares the same letters as the electromagnetic field  
248 strength tensor  $F_{\mu\nu}$ , the additional term  $g_s f^{ABC} \mathcal{A}_\mu^B \mathcal{A}_\nu^C$  in Equation ?? separates QCD  
249 and QED in a very fundamental way: the gluons are allowed to self-interact. This  
250 self-interaction is a direct result of the non-vanishing structure constants of  $SU_c(3)$ <sup>13</sup>,  
251 and is responsible for the challenging nature of QCD calculations.

252 The quarks are represented by the field  $q$ , where the color, flavor and spin indices  
253 have been suppressed. In reality, the quark field  $q$  has:

- 254 • six flavor indices  $\{u, d, s, c, b, t\}$ ,  
255 • four spin indices  $\{0, 1, 2, 3\}$ , and  
256 • three color indices  $\{r, g, b\}$ ,

257 where all of these indices are being implicitly summed over in  $\mathcal{L}_{QCD}$ . Luckily, all of  
258 the matrices  $(\mathcal{A}_\mu^A, \lambda^A, \mathcal{M}, \gamma^\mu)$  act on separate sets of indices<sup>14</sup>. For example, the  $\gamma^\mu$ 's  
259 only operate on the spin indices, whereas both the gluon fields  $\mathcal{A}_\mu^A$  and Gell-Mann  
260 matrices **GellMannEightfold**  $\lambda^A$  operate on the color indices. These Gell-Mann  
261 matrices are the generators of  $SU_c(3)$  and satisfy the commutation relation

$$[\lambda^A, \lambda^B] = 2i f^{ABC} \lambda^C. \quad (1.3)$$

262 The chiral quark fields  $q_L$  and  $q_R$  are defined as  $\frac{1}{2}(1-\gamma_5)q$  and  $\frac{1}{2}(1+\gamma_5)q$ , respectively.  
263 The mass matrix  $\mathcal{M}$  operates on the flavor indices, and its form depends on the choice  
264 of basis for the quark fields **QCDHistory**. It is often convenient to choose a basis

---

<sup>13</sup>Structure constants of Abelian gauge groups like  $U(1)$  are trivially zero.

<sup>14</sup>Really the components of the field corresponding to those indices.

265 where the mass matrix is diagonal, which can be done by independent rotations of  
 266  $q_L$  and  $q_R$  in  $SU(6)$ . Doing so gives the more familiar term

$$-\bar{q}_R \mathcal{M} q_L - \bar{q}_L \mathcal{M}^\dagger q_R = - \sum_{f=1}^6 \bar{q}_f m_f q_f, \quad (1.4)$$

267 where  $m_f$  is the mass of the quark with flavor  $f$ , and  $q_f$  is the flavor component of  
 268 the quark field. Note that this term completely violates the  $SU(2) \times U(1)$  electroweak  
 269 symmetry, indicating that the given  $\mathcal{L}_{QCD}$  is determined *after* the spontaneous sym-  
 270metry breaking described in the previous section.

271 These quark masses are also subject to **renormalization MassRenorm**, which  
 272 is a process that removes the infinities that arise from the self-interaction of the  
 273 quarks and gluons. The renormalization process results in the running of the quark  
 274 masses with respect to the energy scale  $\mu$  of the interaction<sup>15</sup>. More simply, the quark  
 275 masses are inversely dependent on this energy scale: at large  $\mu$ , the quark masses are  
 276 small, and at lower  $\mu$ , the quark masses are large. At the energy scale  $\mu \approx 2$  GeV  
 277 (close to the mass of the proton), the masses of the up, down, and strange quarks—  
 278 collectively referred to as the light-flavor quarks—are approximately  $2.2 \text{ MeV}/c^2$ ,  $4.7$   
 279  $\text{MeV}/c^2$ , and  $96 \text{ MeV}/c^2$ , respectively **PDG**. The heavy-flavor charm, bottom, and  
 280 top quarks have masses of approximately  $1.28 \text{ GeV}/c^2$ ,  $4.18 \text{ GeV}/c^2$ , and  $173 \text{ GeV}/c^2$ ,  
 281 respectively<sup>16</sup>.

282 The final term, known as the  $\theta$ -term **ThetaTerm**, is something of a mystery. It  
 283 is a scalar term that violates CP symmetry **CPSymmetry**, and is often set to zero  
 284 as there is no experimental evidence for its existence. However, it is not clear why  
 285 this term is zero, as there is no symmetry that explicitly forbids it. This is known  
 286 as the **strong CP problem**, and is one of the biggest open questions in particle  
 287 physics **StrongCPPproblem**.

### 288 1.3.1.1 Brief aside: Why eight gluons?

289 The gluon field  $\mathcal{A}^A$  transforms under the adjoint representation of  $SU(3)$ , which  
 290 is a representation of  $SU(3)$  on the vector space of its Lie algebra  $\mathfrak{su}(3)$ . As  $\mathfrak{su}(3)$   
 291 has eight basis elements (for instance, the Gell-Mann matrices  $\lambda^A$  from above), the

---

<sup>15</sup>They also depend on the *choice* of renormalization scheme, with the most commonly implemented one being minimal subtraction or **MS MSScheme**.

<sup>16</sup>At the energy scale governed by their respective masses (i.e.  $\mu = m_Q$ ). **PDG**

292 adjoint representation of SU(3) is eight-dimensional. Thus the gluon field has eight  
293 independent components, or, equivalently, there are eight gluons. In principle, QCD  
294 could have been built on top of a U(3) gauge group, which would give rise to nine  
295 gluons (as the dimension of U(n) is  $n^2$ ). However, the singlet state in U(3) would  
296 be required to be non-interacting; if it were, color neutral baryons would interact  
297 with each other via the strong interaction at a much longer range **SingletGluons**.  
298 Such interactions have not been observed **SingletGluons2**. As there is no physical  
299 difference between U(3) with a non-interacting singlet and SU(3), the simpler gauge  
300 group was chosen.

### 301 1.3.2 Properties of QCD

#### 302 1.3.2.1 Confinement

303 One of the unique properties of QCD is the phenomenon of **confinement**, which  
304 is the observation that quarks and gluons are never seen in isolation. Instead, they  
305 are *confined* inside of the color neutral bound states known as hadrons. This prop-  
306 erty is mostly understood in terms of the coupling constant  $g_s$ . The renormaliza-  
307 tion **QCDRenorm** of QCD gives rise to a  $g_s$  that varies with energy scale or dis-  
308 tance. As the distance between two quarks increases, so too does  $g_s$ . At some point,  
309 the coupling becomes so strong that the energy required to separate the quarks is  
310 enough to create a quark-anti-quark pair from the vacuum. Thus any attempts to  
311 separate a quark from a hadron will always result in the creation of a new hadron,  
312 making it impossible to observe single quarks in isolation.

313 The large coupling constant in this low energy regime makes it impossible to  
314 describe this phenomenon using perturbative techniques, so the exact mechanism of  
315 confinement is still not fully understood. However, it is often described using the  
316 phenomenological Lund string model **LundString**. In this model, the field lines of  
317 two quarks are pulled together due to the self-interaction of the gluons. This creates  
318 a string-like structure between the two quarks, with a potential given by

$$V(r) \approx -\frac{4}{3} \frac{\alpha_s}{r} + \kappa r, \quad (1.5)$$

319 where  $r$  is the distance between the two quarks,  $\alpha_s = \frac{g_s^2}{4\pi}$  and  $\kappa$  is the string tension.  
320 This can be contrasted with the potential between two electrically charged particles,

321 where the field lines are not pulled together and become less dense as the distance  
 322 between the two particles increases. As such, the potential decreases with increasing  
 323 distance, opposite to that of the Lund model. A schematic of these differences can  
 324 be seen in Figure ??.

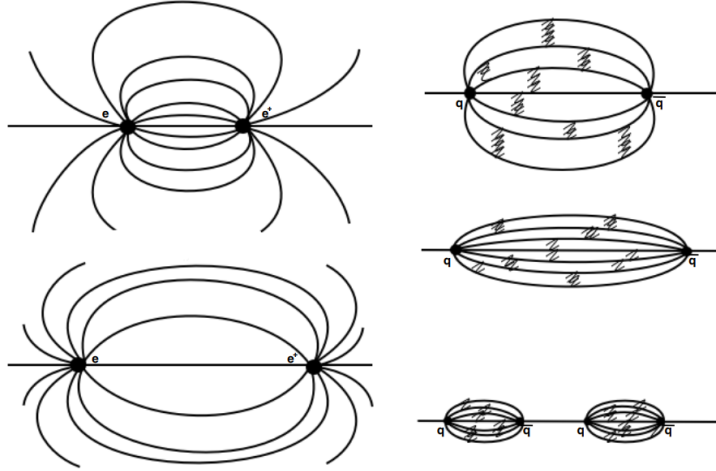


Figure 1.4: A schematic of the field lines between two electrically charged particles (left) and two quarks (right). The field lines between the quarks are pulled together due to the self-interaction of the gluons, whereas the electric field lines are not.

### 325 1.3.2.2 Asymptotic freedom

326 Just as the coupling constant becomes large at low energies and large distances, it  
 327 also becomes small at high energies and small distances. This property is known  
 328 as **asymptotic freedom**: at high enough energies, the quarks and gluons can be  
 329 thought of as “free”, and their interactions can be modeled using perturbative QCD  
 330 (pQCD). As discussed in Section ??, the discovery of asymptotic freedom in QCD  
 331 was what allowed for the accurate predictions of the results of high energy particle  
 332 collision experiments like SLAC **SLAC** and PETRA **PETRA**. The results of such  
 333 experiments have also been used to calculate the value of the coupling constant itself  
 334 at different energy scales, as shown in Figure ???. The value of  $\alpha_s$  at the  $Z^0$  mass is  
 335 also given in the figure, which is the most accurate measurement of  $\alpha_s$  to date **PDG**.

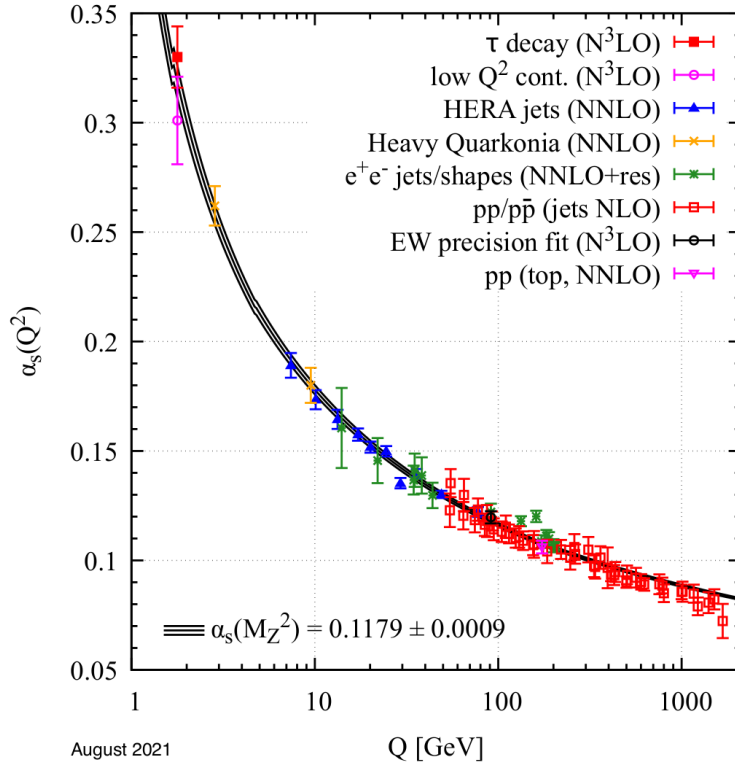


Figure 1.5: The value of the strong coupling constant  $\alpha_s$  as a function of momentum transfer  $Q$ , which represents the energy scale of the interaction.

### 336 1.3.2.3 Chiral symmetry breaking

337 The mass term in the QCD Lagrangian,

$$-\bar{q}_R \mathcal{M} q_L - \bar{q}_L \mathcal{M}^\dagger q_R, \quad (1.6)$$

338 explicitly breaks **chiral symmetry**: swapping the left-handed and right-handed com-  
 339 ponents of the quark fields does not leave the Lagrangian invariant. The breaking of  
 340 chiral symmetry due to the non-zero quark masses is referred to as **explicit** chiral  
 341 symmetry breaking.

342 However, even in the limit of massless quarks, chiral symmetry is broken by the  
 343 QCD vacuum. This is known as **spontaneous** chiral symmetry breaking, and due to  
 344 the non-zero vacuum expectation value of the quark condensate **QuarkCondensate**

$$\langle \bar{q}q \rangle = \langle \bar{q}_L q_R + \bar{q}_R q_L \rangle \neq 0. \quad (1.7)$$

345 This non-zero value is a direct result of the confinement of QCD **TongGaugeTheory**  
346 (Section ??), and implies that the ground state of the theory is filled with quark-anti-  
347 quark pairs. The spontaneous breaking of chiral symmetry in QCD gives rise to eight  
348 massless Nambu-Goldstone bosons **NambuGoldstone**, which are the pseudoscalar  
349 mesons  $\pi^{\pm,0}$ ,  $K^{\pm,0}$ ,  $\eta$ , and  $\eta'$ . These mesons then acquire a small mass due to the  
350 aforementioned explicit chiral symmetry breaking from the quark masses.

351 **1.3.2.4 Jets**

352 During high energy particle collisions (between two protons, for example), the con-  
353 stituent partons of the protons will sometimes scatter off each other in a way that con-  
354 verts most of their initial longitudinal momentum (along the collision axis) into trans-  
355 verse momentum (in the plane perpendicular to the collision axis). Such a scattering  
356 is often referred to as a **hard scattering**. Because the momentum transfer is large,  
357 the cross-section of the parton-parton scattering is calculable using pQCD. Further-  
358 more, branching processes of the high momentum partons—like gluon radiation—can  
359 also be calculated perturbatively. Eventually, however, the partons will lose enough  
360 energy such that their behavior can no longer be described using perturbative tech-  
361 niques.

362 Luckily, the aforementioned Lund model is well-equipped to deal with lower energy  
363 partons. Under the Lund model, as these colored partons move away from each  
364 other, the force between them increases until there is enough energy to produce a  
365 quark-anti-quark pair (as discussed in Section ??). This process—known as string  
366 fragmentation—continues until the partons are no longer energetic enough to move  
367 away from each other, at which point they hadronize into a large number of color  
368 neutral bound states. These particles are roughly collimated in the direction(s) of  
369 the initial hard scattering, forming sprays of hadrons known as **jets**. A diagram  
370 depicting the formation of a jet from an initial hard scattering of partons can be seen  
371 in Figure ??.

372 **1.3.2.5 Flavor conservation**

373 One interesting feature of the interactions in QCD is that all **flavor** quantum numbers  
374 are conserved. Specifically, the number of quarks minus the number of anti-quarks of

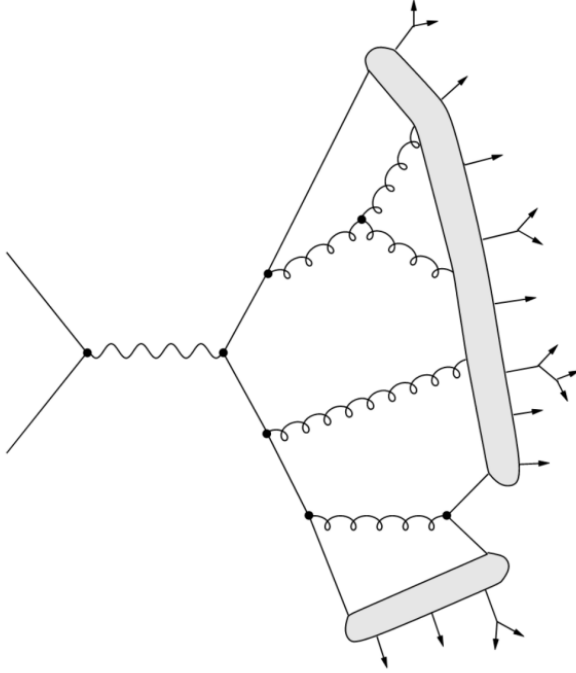


Figure 1.6: A diagram depicting the formation of a jet within the Lund model from an initial hard scattering of partons, adapted from **JetStringDiagram**. The vertices represent perturbative QCD processes, the shaded regions represent string fragmentation/hadronization, and the outgoing arrows represent the resulting hadrons (which may decay further).

375 each flavor is a conserved quantity in every strong interaction<sup>17</sup>. In this thesis, the  
 376 most important flavor quantum number is **strangeness**, which is defined as

$$S = -(n_s - n_{\bar{s}}), \quad (1.8)$$

377 where  $n_s$  is the number of strange quarks and  $n_{\bar{s}}$  is the number of strange anti-quarks.  
 378 The “minus” sign in front of the expression indicates that the strangeness of a strange  
 379 quark is negative ( $-1$ ), and the strangeness of a strange anti-quark is positive ( $+1$ ).  
 380 This convention is chosen<sup>18</sup> to make the signs of these “flavor charges” consistent

---

<sup>17</sup>Conservation of the “historical” flavor quantum number *isospin* (from Section ??), which is  $+\frac{1}{2}$  for up quarks and  $-\frac{1}{2}$  for down quarks, is equivalent to the conservation of  $n_{u,d} - n_{\bar{u},\bar{d}}$  when baryon number is considered. Baryon number is an absolutely conserved quantum number in the Standard Model **PDG**, and (anti-)quarks have baryon number  $(-)\frac{1}{3}$ .

<sup>18</sup>Really this is a historical convention that stems from the fact that “strangeness” was introduced as a concept before the existence of any quark models, as mentioned in Section ??.

381 with the signs of the electric charges of these quarks, which are  $-\frac{1}{3}$  for the strange  
382 quark and  $+\frac{1}{3}$  for the strange anti-quark. Strangeness conservation has an interesting  
383 consequence for particle collisions between atomic nuclei: as the total strangeness of  
384 these nuclei (protons and neutrons) is zero, the number of strange and anti-strange  
385 quarks produced from the strong interaction during these collisions must be equal.  
386 In other words, the production of strange quarks in these collisions must come in the  
387 form of strange quark-anti-quark ( $s\bar{s}$ ) pairs.

## 388 1.4 The Quark-Gluon Plasma

389 One of the consequences of the asymptotic freedom of QCD is the prediction of a new  
390 state of matter at extreme temperatures and densities: the **quark-gluon plasma**  
391 (QGP) **QGP1**, **QGP2**. In this plasma, the quarks and gluons are not confined  
392 inside hadrons, and instead behave as quasi-free particles. This is analogous to an  
393 electromagnetic plasma, where electrons and protons are dissociated from their atoms.  
394 A phase diagram of this plasma can be seen in Figure ???. This diagram has two  
395 axes: temperature and baryon density. Increasing *either* of these quantities beyond  
396 a certain threshold will cause a phase transition from normal hadronic matter to the  
397 QGP. Similarities can be drawn between this phase diagram and that of a snowball:  
398 heating *or* squeezing a snowball will cause it to melt into a liquid<sup>19</sup>.

399 Numerical simulations of QCD on a lattice **LatticeQCD1**, **LatticeQCD2** (known  
400 as lattice QCD or lQCD) have shown that at zero baryon density, the transition from  
401 hadronic matter to the QGP occurs as a smooth crossover **LatticeQCD·Crossover**  
402 with a critical temperature  $T_C \approx 160$  MeV or  $10^{12}$  K, 10,000 times hotter than the cen-  
403 ter of the sun. LQCD has also been used to predict the existence of a critical endpoint  
404 in the QGP phase diagram at a non-zero baryon density **LatticeQCD·CriticalPoint**,  
405 beyond which the transition from hadronic matter to the QGP is no longer a smooth  
406 crossover, but a first-order phase transition. However, due to the complex action  
407 problem **ComplexActionProblem**, lQCD simulations at non-zero baryon density  
408 are not yet possible<sup>20</sup>. Thus the exact location of this critical endpoint is still un-

---

<sup>19</sup>Be careful: if you continue to heat up the snowball enough, or squeeze hard enough, it will undergo another phase transition into the QGP.

<sup>20</sup>Though there are plenty of techniques to extend the lQCD results **TaylorSeries**, **ComplexDensity**, they are only applicable at small baryon densities.

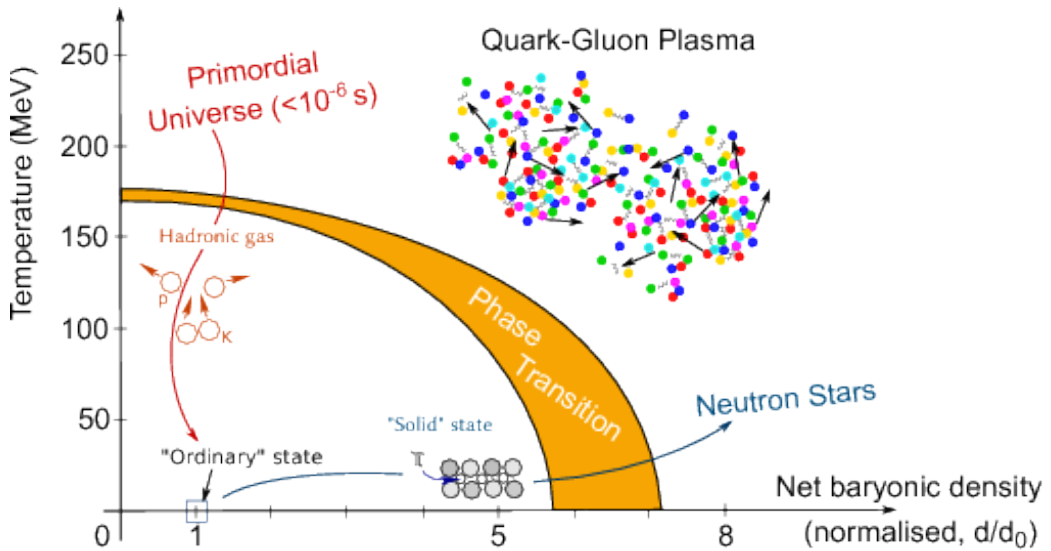


Figure 1.7: A phase diagram of the QGP, taken from [QGPPhaseDiagram](#). The axes are temperature and baryon density, and the orange band represents the phase transition from normal hadronic matter to the QGP.

known, and is the subject of much experimental and theoretical research [QGP3](#).

As the temperatures at the early stages of the universe were well beyond the critical temperature predicted by lQCD, it is thought that the universe was filled with a QGP in the first few microseconds after the Big Bang [QGP3](#). Thus studying the QGP is of interest to cosmologists, as it can give insight to the early universe and its expansion, which is schematically represented in Figure [??](#). It is also postulated that QGP formation occurs in the cores of neutron stars [QGPNeutron](#), giving another avenue of interest for astrophysicists. Furthermore, studying the QGP and its properties can help illuminate the dark, confounding corners of QCD that are not yet understood—like confinement—making it an exciting subject of study for particle physicists. The remainder of this section will discuss the theoretical characteristics of this interesting plasma.

#### 1.4.1 Properties of the QGP

##### 1.4.1.1 Deconfinement

The most defining characteristic of the QGP is that the quarks and gluons within the plasma are not confined inside hadrons, and instead interact as quasi-free particles.

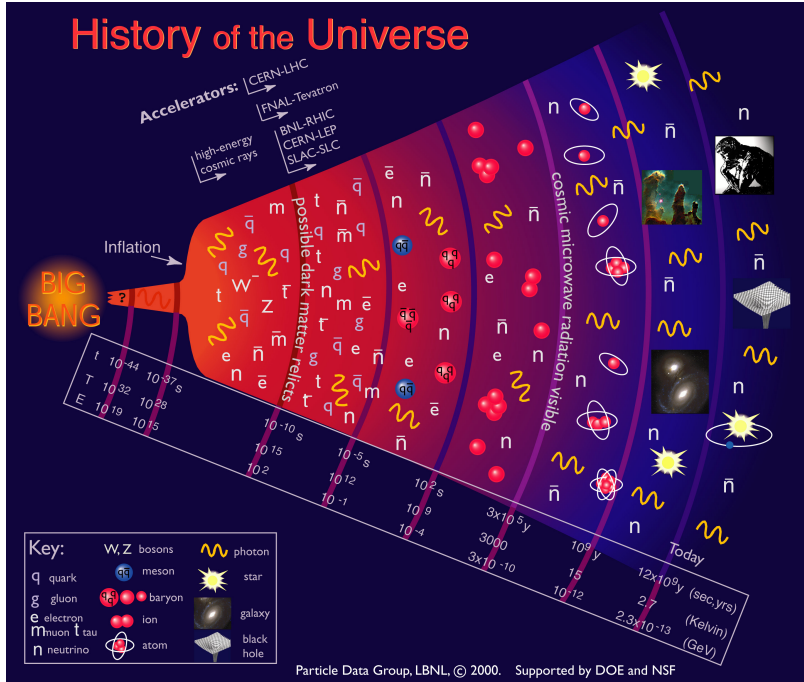


Figure 1.8: A schematic of the evolution of the universe, taken from **PDG**. The QGP phase of the universe on this diagram lies roughly between  $10^{-10}$  and  $10^{-5}$  seconds after the Big Bang.

As mentioned in Section ??, the coupling constant  $g_s$  becomes smaller with increasing energies. At high enough energies, the coupling constant becomes small enough that the quarks and gluons become deconfined. In lQCD, the order parameter for deconfinement is the Polyakov loop expectation value **PolyakovLoop**  $\langle L \rangle$ , which is zero in the confined phase and greater than zero in the deconfined phase. This transition, from  $\langle L \rangle = 0$  to  $\langle L \rangle > 0$ , is used<sup>21</sup> to define the transition from hadronic matter to the QGP.

#### 1.4.1.2 Chiral symmetry restoration

As mentioned in Section ??, the QCD vacuum has a non-zero quark condensate  $\langle q\bar{q} \rangle$  which spontaneously breaks chiral symmetry. However, this non-zero condensate is the direct result of the confinement of QCD **TongGauge**. Thus, in the QGP—

---

<sup>21</sup>Technically the more common order parameter is the quark condensate discussed in the next section, but the critical temperatures predicted by lQCD using these different order parameters are usually very similar **QCDOOrderParameterSimilarity**.

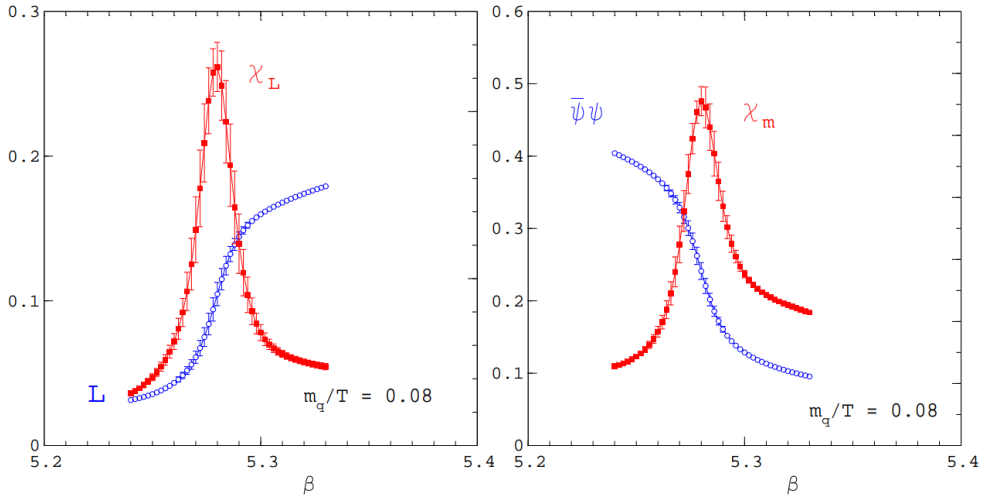


Figure 1.9: The deconfinement order parameter  $\langle L \rangle$  and chiral symmetry order parameter  $\langle \bar{q}q \rangle$  (along with their corresponding susceptibilities) as a function of the coupling  $\beta = 6/g_s^2$  using 2-flavor 1QCD, taken from **FrithofLattice**. The critical temperatures (indicated by the maxima of the susceptibilities) occur at roughly  $\beta = 5.28$ , corresponding to a temperature of around 170 MeV.

where the quarks and gluons are no longer confined—the quark condensate should vanish. As such, another defining characteristic of the QGP is the restoration of the spontaneously broken chiral symmetry of QCD, often referred to as **chiral symmetry restoration**. This transition, from  $\langle \bar{q}q \rangle > 0$  to  $\langle \bar{q}q \rangle = 0$ , is also used to define the QGP phase transition.

An 1QCD diagram of the deconfinement order parameter  $\langle L \rangle$  and chiral symmetry order parameter  $\langle \bar{q}q \rangle$  (along with their corresponding susceptibilities) as a function of the coupling  $\beta = 6/g_s^2$  can be seen in Figure ???. Note that the susceptibilities are maximal at the same coupling value (corresponding to a critical temperature of around 170 MeV), indicating that both deconfinement and chiral symmetry restoration correspond to the same phase transition, namely the transition from hadronic matter to the QGP.

#### 1.4.1.3 Hydrodynamic behavior

The QGP is a strongly interacting plasma. As such, it is expected to exhibit fluid-like behavior at a macroscopic level. Unfortunately, the calculation of QGP transport coefficients from first principles using QCD is very difficult **FlowViscPaper**. Us-

452 ing perturbative techniques to calculate the shear and bulk viscosities of the QGP  
 453 results in values that are an order of magnitude larger than those extracted from  
 454 experimental data **Visc1**, **Visc2**. The extraction of these transport coefficients us-  
 455 ing lQCD is also challenging, as the aforementioned complex action problem makes  
 456 it nearly impossible to simulate the QGP at non-zero baryon density. The most  
 457 promising approach to calculating these transport coefficients is through the use of  
 458 the AdS/CFT correspondence **AdSCFT**, which is a duality between a strongly cou-  
 459 pled gauge theory (like QCD) and a weakly interacting gravitational theory (like  
 460 string theory **StringTheory**). This approach has been used to approximate the  
 461 lower bound of the shear viscosity of a strongly-coupled medium **QGPViscADS**,

$$\eta/s \approx 1/4\pi, \quad (1.9)$$

462 which is often described as the shear viscosity of a “perfect fluid” **PerfectFluid**.  
 463 Experimental evidence suggests that the QGP has a shear viscosity that is very close  
 464 to this lower bound **QGPViscExp**, indicating that it is a nearly perfect fluid.

#### 465 1.4.1.4 Radiative energy loss

466 Partons traveling through the QGP lose energy through both collisional and radiative  
 467 processes, as shown in Figure ???. The collisional energy loss is due to elastic scattering  
 468 between the partons and the constituents of the QGP. For a parton with energy  $E$   
 469 much greater than its mass and the temperature of the QGP, the collisional energy  
 470 loss is given by **GluonRadiation**

$$\Delta E_{\text{coll}} \sim \alpha_s^2 T^2 L, \quad (1.10)$$

471 where  $T$  is the temperature of the QGP and  $L$  is the length of travel through the  
 472 medium (which is assumed to be larger than the critical length  $L_{cr} \sim \frac{1}{\alpha_s T} \sqrt{\frac{E}{T}}$ ).  
 473 The radiative energy loss is due to gluon radiation induced by the presence of the  
 474 medium<sup>22</sup>. Again, for a parton with  $E \gg M, T$ , the radiative energy loss is given  
 475 by **GluonRadiation**

$$\Delta E_{\text{rad}} \sim \alpha_s^2 \sqrt{ET^3} L, \quad (1.11)$$

476 where  $E$  is the energy of the parton. As the radiative energy loss is proportional  
 477 to  $\sqrt{E}$ , it is the dominant energy loss mechanism for light, energetic partons (i.e.

---

<sup>22</sup>Similar to bremsstrahlung, where electrically charged particles radiate photons in the presence of other charged particles.

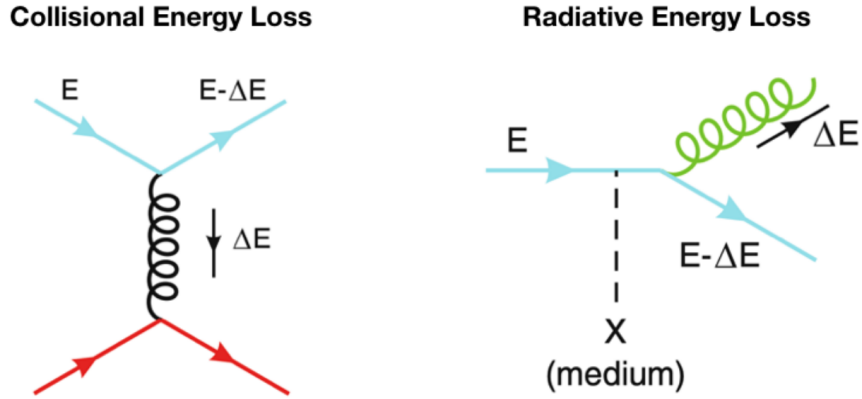


Figure 1.10: A diagram depicting the collisional (left) and radiative energy loss (right) processes of a parton traveling through the QGP. Radiative energy loss is the dominant energy loss mechanism for all energetic partons in the QGP.

478  $u$ ,  $d$ , and  $s$  quarks as well as gluons). However, gluons lose more energy than the  
 479 light quarks due to their larger color charge. The heavier quarks are expected to  
 480 lose less energy through radiative processes due to the *dead cone effect*, whereby the  
 481 gluon radiation is suppressed in the forward direction due to the larger masses of the  
 482 heavy quarks **DeadCone**. Even still, the radiative energy loss of heavy quarks is  
 483 larger than their collisional energy loss **DeadCone**, making radiative energy loss the  
 484 dominant energy loss mechanism for all energetic partons in the QGP.

#### 485 1.4.2 Enhanced $s$ -quark production

486 In the context of the research presented in this thesis, the most important character-  
 487 istic of the QGP is the increase in the production of strange quarks relative to the  
 488 production of up and down quarks **Strangeness**. Discovered in 1981 by physicists  
 489 Johann Rafelski and Rolf Hagedorn, this *enhancement* in the production of strange  
 490 quarks in the QGP is often referred to as **strangeness enhancement**. As mentioned  
 491 in Section ??, strangeness is conserved during strong interactions. As such, the pro-  
 492 duction of  $s\bar{s}$  pairs can only come from four Feynman diagrams (to lowest order in  
 493 pQCD), shown in Figure ???. A key insight made by Rafelski and Hagedorn is that  
 494 in the QGP, the higher temperatures allow for the thermal production of  $s\bar{s}$  pairs  
 495 through gluon fusion ( $gg \rightarrow s\bar{s}$  or diagrams (a) (b) and (c) in Figure ???). This gluon

496 fusion occurs much faster than the quark-based production ( $q\bar{q} \rightarrow s\bar{s}$  or diagram (d)  
 497 in Figure ??), and allows for the full chemical equilibration of strangeness in the QGP  
 498 in less than  $10^{-24}$  seconds. Strangeness equilibration in a hadronic gas, on the other  
 499 hand, takes much longer: on the order of  $10^{-10}$  seconds **Strangeness**.

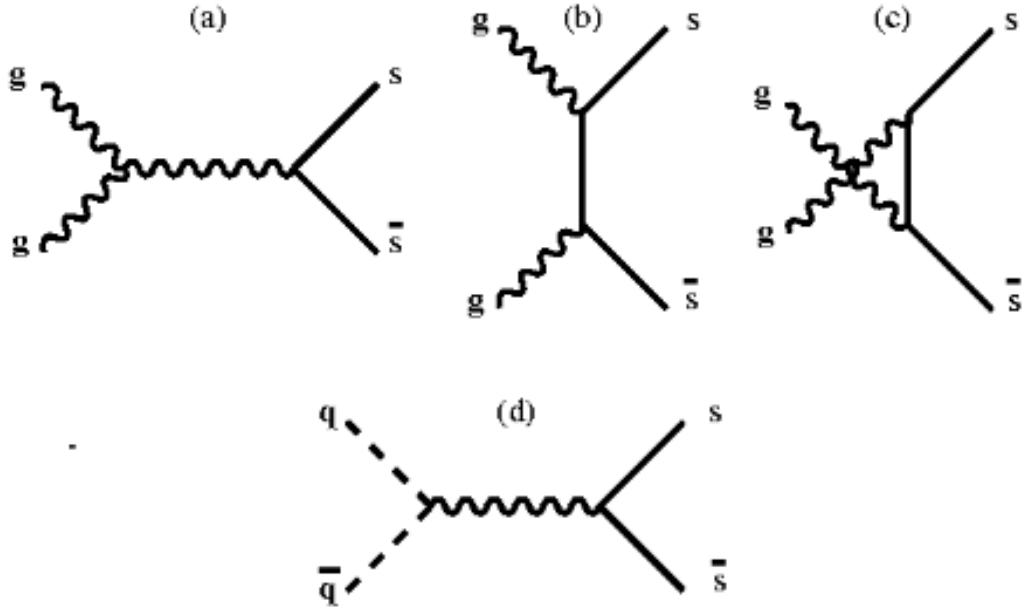


Figure 1.11: The four leading-order Feynman diagrams responsible for the production of  $s\bar{s}$  pairs in the QGP, adapted from **Strangeness**. Diagrams (a), (b) and (c) are the gluon fusion processes, while diagram (d) is the quark-based process.

#### 500 1.4.2.1 Statistical hadronization

501 The production of strangeness in the QGP and within a hadron gas is often described  
 502 in terms of the **statistical hadronization model** (SHM). The SHM is based off of  
 503 the Fermi model of hadron formation, where it is assumed that the strong interactions  
 504 saturate the quantum particle production matrix elements **RafelskiStatisticalH**.  
 505 This assumption allows for the calculation of the particle yields using only conser-  
 506 vation laws and the available phase space, while ignoring the unknown microscopic  
 507 details of the hadronization process. In the fundamental micro-canonical approach  
 508 for the SHM, the available phase space is determined by the energy density of lo-  
 509 calized “clusters” within the system. However, a grand canonical framework for the

510 SHM is often used for highly energetic systems, where the phase space is determined  
 511 by a global temperature-like parameter  $T$ .

512 The most important quantity for describing particle yields within the grand canonical  
 513 SHM is the particle fugacity  $\lambda_i$ , which is defined as

$$\lambda_i = e^{\mu_i/T}, \quad (1.12)$$

514 where  $\mu_i$  is the chemical potential of particle  $i$ . In essence, the fugacity “counts” the  
 515 number of particles of type  $i$  in the system **Strangeness**. For systems in absolute  
 516 chemical equilibrium, the chemical potentials for particle and anti-particle flavors  
 517 are opposite to each other. Consequently, the relationship between the particle and  
 518 anti-particle fugacities is given by

$$\lambda_{\bar{i}} = \lambda_i^{-1}. \quad (1.13)$$

519 However, this relationship does not hold for systems that have not reached absolute  
 520 chemical equilibrium, as the chemical potentials of the particle and anti-particle fla-  
 521 vors are no longer opposite to each other. Due to the higher mass of the strange  
 522 quark, the production of  $s\bar{s}$  pairs usually proceeds at a much slower rate than the  
 523 production of  $u\bar{u}$  and  $d\bar{d}$  pairs. As such, obtaining absolute chemical equilibrium for  
 524 strange particles is difficult, especially in hadronic matter<sup>23</sup>.

525 To account for this, the SHM introduces the concept of *relative* chemical equilib-  
 526 rium, in which the strange phase space is not fully saturated, but whatever strangeness  
 527 is produced is distributed among the strange hadron channels according to the law of  
 528 maximum entropy **9212210·hep-ph**. The extent to which the strange phase space  
 529 is saturated is parameterized by  $0 < \gamma_s \leq 1$ , which gives a modified particle fugacity,

$$\lambda_i^{\text{mod}} = \gamma_s^{n(i,s)} \lambda_i, \quad (1.14)$$

530 where  $n(i,s)$  is the number of strange quarks plus the number of strange anti-quarks  
 531 in particle  $i$ . The factor  $\gamma_s$  approaches unity whenever the strange phase space is fully  
 532 saturated (i.e. when the system is in absolute chemical equilibrium). This factor can  
 533 be determined by looking at strange particle ratios, which are sensitive to the value  
 534 of  $\gamma_s$ . For example, the ratio of  $\Lambda$  baryons to protons is related to  $\gamma_s$  by

$$\gamma_s^2 = \frac{\Lambda}{p} \times \frac{\bar{\Lambda}}{\bar{p}}. \quad (1.15)$$

---

<sup>23</sup>As mentioned in the previous section, strangeness equilibration in a hadronic gas is over X times slower than in the QGP

535 As these particle ratios can be measured by particle collision experiments, it is  
536 possible to determine the value of  $\gamma_s$  for a given collision system. Measuring  $\gamma_s$  in  
537 heavy-ion collisions is of particular interest, as it is believed that the QGP is formed  
538 in these collisions. However, heavy-ion collisions are very short-lived systems, lasting  
539 only around  $10^{-23} - 10^{-22}$  seconds **QGPFormation**. As mentioned previously, full  
540 chemical equilibration in a hadronic gas cannot occur within this time frame. As  
541 such, measuring values of  $\gamma_s$  close to unity in heavy-ion collisions would be a strong  
542 indication of QGP formation.

543 **1.5 Using Heavy-Ion Collisions to Study the**  
544 **QGP**

545 The QGP phase diagram in Figure ?? shows two methods for producing the QGP:  
546 increasing the system's temperature or increasing its baryon density. Luckily these  
547 two methods are not mutually exclusive:

- 548 • Baryon density can be increased by looking at systems with a lot of baryons  
549 packed together (like the nucleus of a lead atom)
- 550 • Temperature can be increased by smashing the aforementioned systems together  
551 at higher energies (like in a particle accelerator)

552 Thus one of the best (and only) ways to study the QGP in a laboratory setting is  
553 through relativistic **heavy ion collisions**: the smashing together of two heavy nuclei  
554 at very high energies using a particle accelerator.

555 Unfortunately, producing the QGP in this manner has a major drawback; while  
556 it is possible to heat up the system beyond the critical temperature required for  
557 QGP formation, the system expands and cools *very* quickly. For example, the QGP  
558 produced by colliding lead ions with center-of-mass energy  $\sqrt{s_{NN}} = 2.76$  TeV at the  
559 Large Hadron Collider (LHC) only lasts for around  $3 \text{ fm}/c$  **QGPFormation**, or  $10^{-23}$   
560 seconds. A diagram depicting the formation and evolution of the QGP in a heavy ion  
561 collision can be seen in Figure ?? . This diagram can be split up into the following  
562 stages:

- 563     1. The Lorentz-contracted nuclei approach each other at very high energies, and  
564       the partons within the nuclei scatter off each other ( $t = 0 \text{ fm}/c$ ).  
  
565     2. As new partons are created from the initial scatterings, the energy density of  
566       the system increases. Eventually this energy density is high enough to create  
567       the QGP ( $t \approx 1 \text{ fm}/c$ ).  
  
568     3. Once the QGP is formed, it expands and cools in a hydrodynamic manner.  
  
569     4. After the QGP cools below the critical temperature, the partons begin to  
570       hadronize, resulting in the formation of a hadron gas ( $t \approx 3 \text{ fm}/c$ ).  
  
571     5. The hadron gas will continue to expand until the hadrons within the gas are no  
572       longer strongly interacting with each other ( $t \approx 10 \text{ fm}/c$ ). This is often broken  
573       up into two stages:  
  
574       • The hadrons cease to interact *inelastically*, called **chemical freeze-out**.  
575       • The hadrons cease to interact *elastically*, called **kinetic freeze-out**.  
  
576     6. If a detector is built within a few meters around the collision point, the final  
577       state hadrons can be observed ( $t \approx 10^{15} \text{ fm}/c$ ).

578     The last stage of this diagram is perhaps the most frustrating: it is only possible  
579     to study the QGP by observing the final state hadrons. Luckily, there are some  
580     key observables associated with those final state hadrons that can shed light on the  
581     formation and evolution of this exciting plasma. Before those observables can be  
582     discussed, however, it is necessary to introduce a key concept in heavy ion collisions:  
583     the centrality of the collision.

### 584     1.5.1 Collision centrality

585     The very first step of the heavy ion collision process involves the scattering of the  
586     partons within the two nuclei. However, these nuclei are not point-like objects: they  
587     have a finite size, and therefore need not collide “head-on”. Instead, the nuclei  
588     can collide at different **impact parameters** (commonly denoted as  $b$ ), as shown  
589     in Figure ???. The impact parameter is defined as the distance between the centers  
590     of the two nuclei, measured in the transverse plane (the plane perpendicular to the

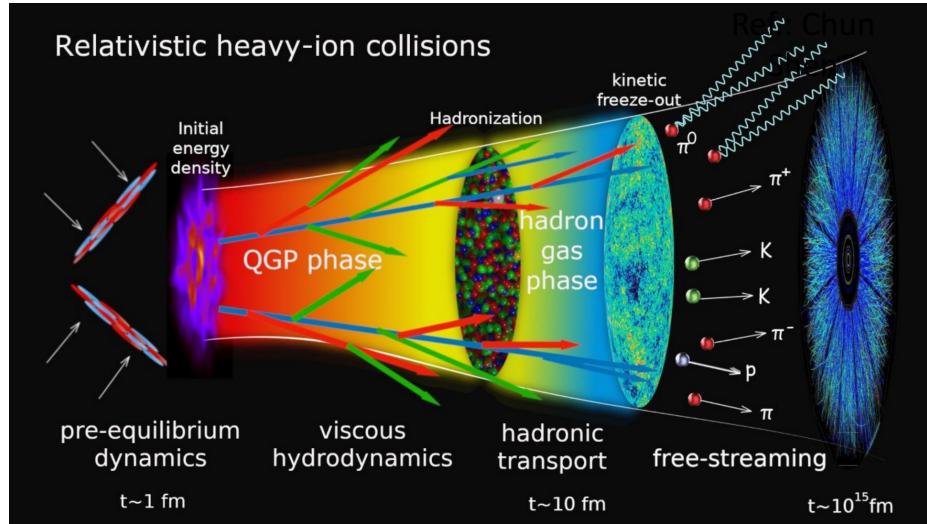


Figure 1.12: A schematic of the formation and evolution of the QGP in a heavy ion collision. The QGP is formed in the overlap region of the two colliding nuclei, and then expands and cools very quickly.

591 initial directions of the nuclei). Collisions with a large impact parameter give rise to  
 592 *spectator* nucleons, which do not participate in the collision and continue traveling  
 593 as they please.

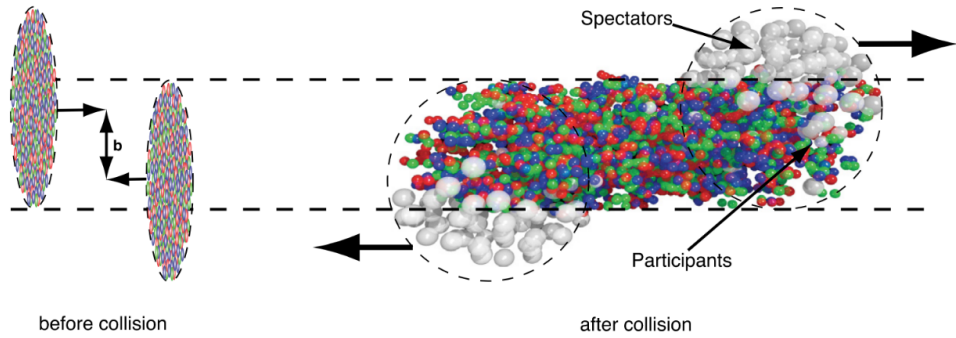


Figure 1.13: A schematic of a heavy ion collision with impact parameter  $b$ , taken from **CERNCourierImpactParam**.

594 The impact parameter is very important when studying the QGP for a fairly  
 595 straightforward reason: as the impact parameter decreases, the number of partonic  
 596 scatterings increases, which in turn increases the energy density of the system. In  
 597 some sense, the size of the impact parameter determines whether or not the QGP is

598 formed in the subsequent stages of the collision. As such, characterizing heavy ion  
 599 collisions by their impact parameter is quite useful. Unfortunately, much like the  
 600 QGP, the impact parameter is not directly measurable and must be inferred from the  
 601 final state hadrons.

602 Instead of classifying collisions based off their unobtainable impact parameter,  
 603 they are instead classified by their **collision centrality**. The collision centrality is  
 604 defined as

$$c = \frac{\int_0^b d\sigma/db' db'}{\int_0^\infty d\sigma/db' db'} = \frac{1}{\sigma_{AA}} \int_0^b \frac{d\sigma}{db'} db', \quad (1.16)$$

605 where  $\sigma_{AA}$  is the total cross section of the nucleus-nucleus (A-A) collision. As this  
 606 number is strictly between 0 and 1, it is often expressed as a percentile: 0% corre-  
 607 sponds to the most central collisions (lowest impact parameters), and 100% corre-  
 608 sponds to the most peripheral collisions (highest impact parameters). If a monotonic  
 609 relationship between  $b$  and the number of final state particles seen in the detector is as-  
 610 sumed, the collision centrality can be experimentally determined **GlauberModelALICE1**.  
 611 The number of final state particles from a collision is called the **multiplicity** of the  
 612 collision, and is often denoted as  $N_{ch}$ . The subscript  $ch$  indicates that only charged  
 613 particles are counted, as neutral particles are not seen by most detectors.

614 In practice, the collision centrality percentiles are usually determined by looking  
 615 at the distribution of events as a function of the signal (effectively  $N_{ch}$ ) as measured  
 616 by a particular detector. The percentile for a specific event can then be determined  
 617 by integration:

$$c \approx \frac{1}{\sigma_{AA}} \int_{N_{ch}}^\infty \frac{d\sigma}{dN'_{ch}} dN'_{ch}, \quad (1.17)$$

618 where  $N_{ch}$  is the multiplicity of the event in question. An example of separating  
 619 events into centrality percentiles using this method can be seen in Figure ???. In  
 620 this plot, Pb–Pb collisions are characterized by their event activity in the ALICE  
 621 VZERO detector (which will be discussed in more detail in the next chapter). The  
 622 red points correspond to fits obtained using Monte Carlo simulations based off of the  
 623 Glauber model **GlauberModelALICE1**, **GlauberModelALICE2**. The Glauber  
 624 model **GlauberModel** is a geometric model that treats the nuclei as a collection  
 625 of nucleons, and models the collisions as a superposition of binary nucleon-nucleon  
 626 collisions. This model gives a relationship between the impact parameter  $b$ , the  
 627 number of participating nucleons  $N_{part}$ , and the number of binary nucleon-nucleon

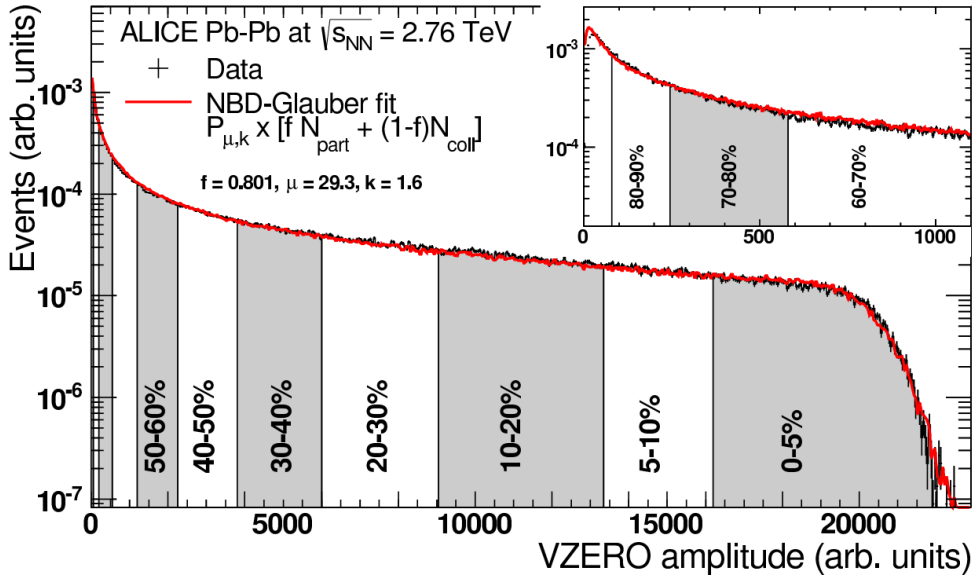


Figure 1.14: The distribution of Pb–Pb collision events as a function of event activity in the ALICE VZERO detector, taken from **GlauberModelALICE2**.

628 collisions  $N_{coll}$ . While not of particular import to this thesis, fitting the Glauber  
 629 model to the data actually allows for the determination of the impact parameter  
 630 corresponding to a given multiplicity percentile. The fact that the model describes  
 631 the data well also serves as a sanity check for the experimental estimation of the  
 632 collision centrality. In this thesis, the terms “multiplicity percentile” and “collision  
 633 centrality” will be used interchangeably.

634 The approximation given by Equation ?? has an additional benefit: it allows for  
 635 the determination of centrality without a clearly defined impact parameter. This is  
 636 useful for proton-proton and proton-lead collisions, where the impact parameter is  
 637 ill-defined.

## 638 1.6 Experimental signatures of QGP formation

639 As mentioned in Section ??, the QGP produced within a heavy ion collision is *very*  
 640 short lived. As such, any attempt to study the QGP and its formation must be  
 641 done using the detector-accessible final state hadrons. Luckily there are a number of  
 642 signatures that can be used to study the QGP in experiment, including

- 643 • **jet quenching** **JetQuenching**, where the energy of a jet is heavily reduced  
644 due to its interactions with the QGP,
- 645 • **collective flow** **CollectiveFlow**, where the motion of the partons within the  
646 QGP is heavily influenced by the overall fluid-like medium, and
- 647 • **strangeness enhancement** **Strangeness**, where the QGP exhibits an in-  
648 crease in the production of strange quarks relative to up and down quarks.

649 These signatures are discussed in more detail in the following sections.

### 650 1.6.1 Jet quenching

651 The high momentum partons produced in the initial hard scatterings of heavy ion  
652 collisions often traverse the QGP medium. Much like electron tomography, where  
653 the passage of electrons through an atomic medium can give insight to the structure  
654 of the atoms within, these high momentum partons can be used to probe the QGP.  
655 These colored partons interact with the colored medium, losing energy in the process.  
656 As discussed in Section ??, these partons are never observed individually; instead,  
657 they hadronize into a spray of particles known as a jet. Thus the energy lost by  
658 the parton is not observed directly, but rather as a reduction in the energy of the  
659 resulting jet. This phenomenon is known as **jet quenching**, and is one of the most  
660 well studied signatures of QGP formation.

661 Experimentally, this quenching is observed by studying *dijets*. While the term  
662 “jet” refers to a single spray of particles observed in the detector, the initial hard  
663 scattering responsible for the formation of the jet corresponds to the production of  
664 *two* high momentum partons. Traveling in opposite directions in the transverse plane,  
665 these partons often produce two jets that are back-to-back in  $\varphi$  (the azimuthal angle  
666 in the transverse plane). These two jets are collectively referred to as a dijet. In pp  
667 collisions, the energy of the two jets is roughly equal as the corresponding partons  
668 don’t lose energy to a medium. In heavy ion collisions, however, the partons lose  
669 energy to the QGP due to gluon radiation and elastic scattering with the medium’s  
670 constituents **JetQuenchingReview**. If one of the two partons has a larger path  
671 length through the QGP, it will lose more energy than the other parton, resulting in  
672 an imbalance in the energy of the two jets. A schematic of this process for pp and  
673 A–A collisions can be seen in Figure ??.

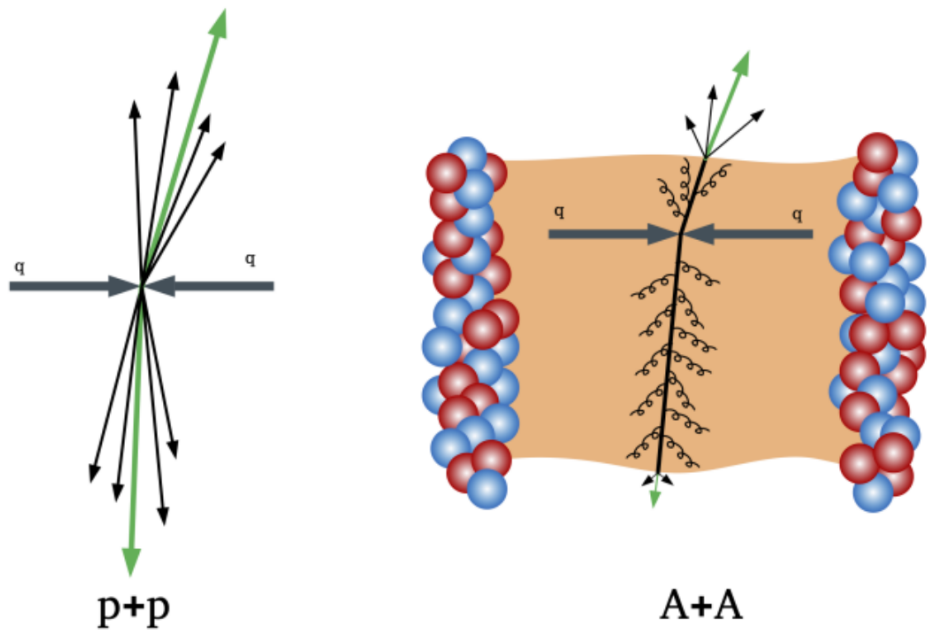


Figure 1.15: A schematic of the formation of dijets in  $p+p$  and  $A-A$  collisions, taken from [DijetSchematic](#).

674 However, the path length within the QGP of the dijet-forming partons should be  
 675 roughly uniform, washing out this assymetry over a large event sample. As such, jet  
 676 quenching is experimentally observed by selecting high momentum “trigger” hadrons,  
 677 which most likely originated from the parton with the smaller QGP path length. The  
 678 jet corresponding to this higher momentum trigger—referred to as the “near-side” jet—  
 679 is then compared with its partner jet, which would be  $180^\circ$  away in azimuth—called the  
 680 “away-side” jet. The first collaboration to observe this jet quenching was the STAR  
 681 collaboration at the Relativistic Heavy Ion Collider (RHIC) **STARJetQuenching**.  
 682 By looking at high transverse momentum hadrons produced in Au–Au collisions, they  
 683 found that the away-side jet began to “disappear” as the centrality of the collision  
 684 increased, as shown in Figure ???. This disappearance is due to the away-side jet  
 685 losing energy to the QGP, such that the corresponding hadrons in the away-side fall  
 686 below the momentum cutoff.

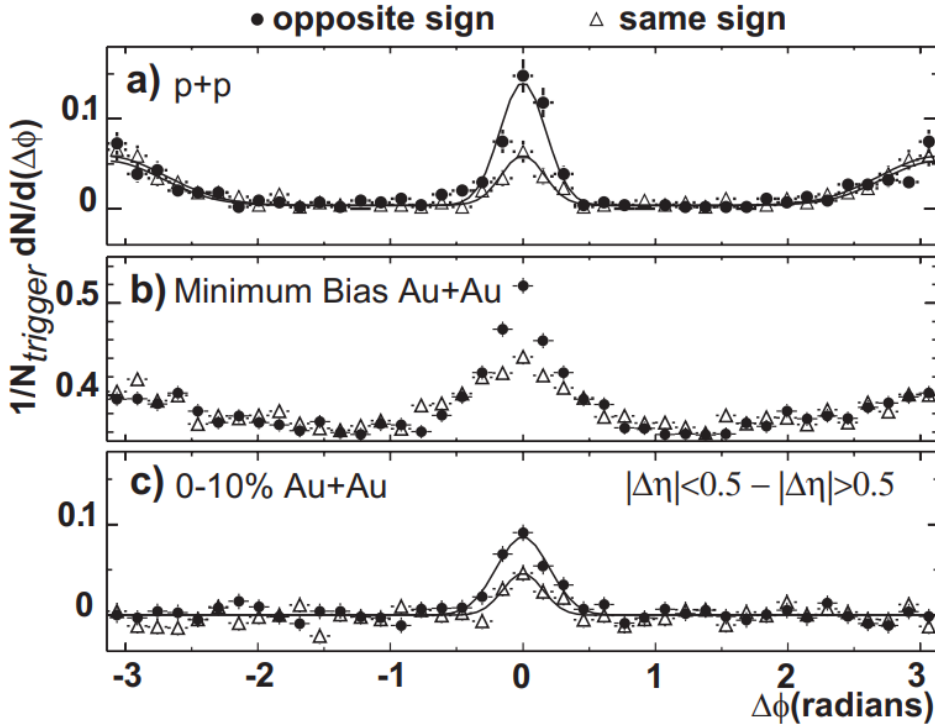


Figure 1.16: Hadron yields corresponding to the near-side jet (near  $\Delta\varphi = 0$ ) and the away-side jet ( $\Delta\varphi = \pm\pi$ ), taken from **STARJetQuenching**. In pp and minimum bias Au+Au collisions, the away-side jet is present. However, at high centrality (0-10%), the away-side jet completely disappears.

### 687 1.6.2 Collective flow

688 The QGP is a strongly interacting medium, whose constituent partons are heavily  
 689 coupled to their surroundings. Just as the pebbles within a river get swept up in  
 690 the flow of the water, the partons within the QGP are influenced by the flow of this  
 691 medium. This flow manifests itself by the presence of collective effects in the final  
 692 state hadrons, which are often quantified using **collective flow** components. These  
 693 flow components are obtained by expanding the final state hadron distribution in a  
 694 Fourier series with respect to the azimuthal angle  $\phi$  **Flow24**,

$$E \frac{d^3 N}{d^3 p} = \frac{1}{2\pi} \frac{d^2 N}{p_t dp_t dy} \left( 1 + \sum_{n=1}^{\infty} 2v_n \cos [n(\phi - \Psi_R)] \right), \quad (1.18)$$

695 where  $E$  is the energy of the particle,  $p$  is its momentum,  $p_T$  is the momentum  
 696 component in the plane transverse to the beam axis,  $y$  is the particle's rapidity, and  
 697  $\Psi_R$  is the reaction plane angle. This reaction plane angle is defined by the beam axis  
 698 and the impact parameter vector. The Fourier coefficients

$$v_n = \langle \cos[n(\phi - \Psi_R)] \rangle \quad (1.19)$$

699 determine the “strength” of the corresponding flow component. The first two co-  
 700 efficients,  $v_1$  and  $v_2$ , are referred to as **directed (radial) flow** and **elliptic flow**,  
 701 respectively. A non-zero directed flow originates from the space-momentum corre-  
 702 lations in particle production from a longitudinally slanted source **DirectedFlow**.  
 703 Directed flow is often much smaller than elliptic flow (by over an order of magni-  
 704 tude) **DirectedFlow2**, but it can still effect some of the measurements presented in  
 705 this thesis (see Section ?? for more details).

706 Elliptic flow characterizes the anisotropy of the particle production in the trans-  
 707 verse plane. This anisotropy is believed to be caused by the initial anisotropy of the  
 708 collision geometry, where the overlap region of the colliding nuclei forms an “almond”  
 709 shape. This almond is where the initial QGP is formed, which then hydrodynamically  
 710 expands and thermalizes nearly instantaneously. The initial spacial anisotropy results  
 711 in unequal QGP path lengths for the constituent partons, which ultimately results in  
 712 an anisotropic momentum distribution for the corresponding hadrons (i.e. partons  
 713 which travel through more medium lose more energy, as discussed in Section ??). A  
 714 diagram depicting this process can be seen in Figure ??.

### 715 1.6.2.1 Avoiding $\Psi_R$

716 Reconstructing the reaction plane angle  $\Psi_R$  is difficult as it must be done on an event-  
 717 by-event basis **Flow24**. As such, it is often more convenient to measure the collective  
 718 flow components by looking at two-particle correlations in the azimuthal angle  $\phi$ . In  
 719 other words, the flow components can be obtained by looking at the distribution of  
 720 pairs of particles as a function of  $\Delta\phi = \phi_1 - \phi_2$ , where  $\phi_1$  and  $\phi_2$  are the azimuthal  
 721 angles of two (non-identical) particles. This distribution can be decomposed into a  
 722 Fourier series similar to Equation ?? **FlowDphi**,

$$\frac{dN^{\text{pair}}}{d\Delta\varphi} = a_0 + 2a_1 \cos \Delta\varphi + 2a_2 \cos 2\Delta\varphi + \dots, \quad (1.20)$$

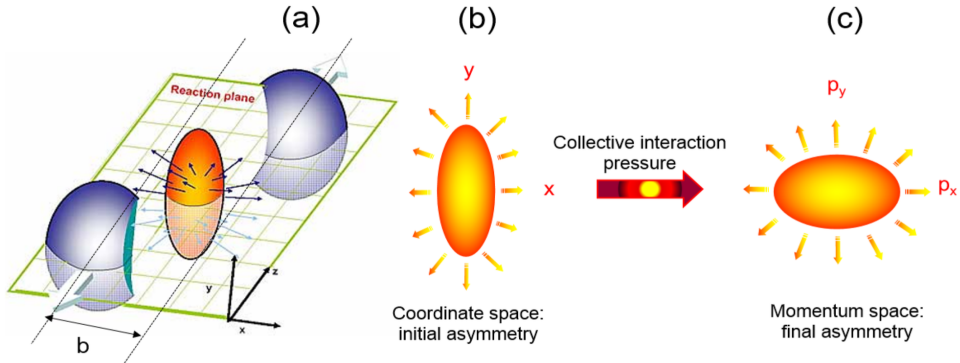


Figure 1.17: A schematic of the formation of elliptic flow in a heavy ion collision. The initial anisotropy in coordinate space results in a pressure gradient that causes a momentum space anisotropy in the final state hadrons.

723 where  $v_n \equiv a_n/a_0$  are the very same flow coefficients from before. This bypasses the  
 724 need to reconstruct the reaction plane angle  $\Psi_R$ , but it also makes clear that any  
 725 analyses involving two-particle angular correlations (like the one presented in this  
 726 thesis) must be mindful of the presence of these coefficients (see Chapter ?? for more  
 727 details).

### 728 1.6.3 Strangeness enhancement

729 Experimentally, strangeness production is measured by looking at the abundance  
 730 of strange hadrons relative to non-strange hadrons, like pions. For central heavy  
 731 ion collisions—both at the LHC and RHIC—these strange/non-strange particle ratios  
 732 are found to be consistent with a hadron gas in both thermal *and* chemical equilib-  
 733 rium **NATURE12, NATURE13**. As mentioned previously, this is a strong indi-  
 734 cation that the QGP is formed in these collisions. Furthermore, these particle ratios  
 735 as measured in lower multiplicity pp collisions at the LHC are found to be consistent  
 736 with statistical models *without* chemical equilibration **NATURE14, NATURE15**.  
 737 Under the strangeness enhancement picture, this indicates that QGP formation does  
 738 *not* occur in these lower multiplicity pp collisions.

739 However, filling in the gaps between low multiplicity pp collisions and high mul-  
 740 tiplicity Pb–Pb collisions reveals a more complicated picture, as shown in Figure ??.  
 741 The particle ratios seem to be consistent with a smooth transition between the two

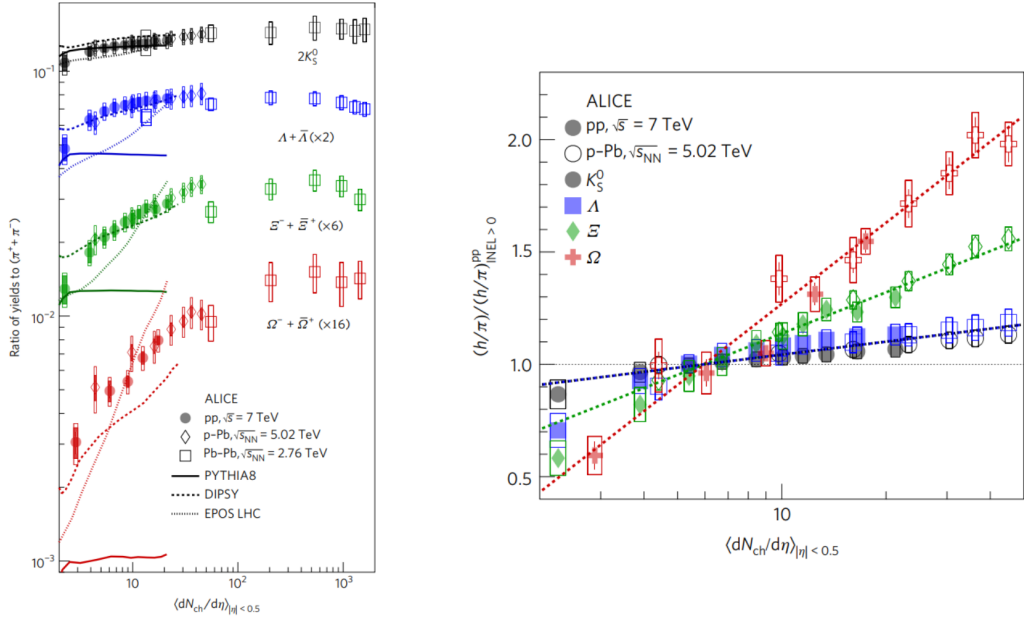


Figure 1.18: The particle ratios of strange hadrons to pions as a function multiplicity for different collision systems (left) and those same ratios normalized to an inclusive pp sample (right). The ratios appear to only depend on the multiplicity of the collision, and not the collision system. Taken from **NATURE**.

regimes, independent of collision system. In other words, the ratios in higher multiplicity pp and p–Pb collisions match up nicely with the ratios in lower multiplicity Pb–Pb collisions. This indicates that the enhanced production of strange quarks is not exclusive to heavy ion collisions; there is an “onset” of strangeness enhancement occurring in lower multiplicity pp and p–Pb collisions. Furthermore, this enhancement is seen to scale with the number of strange quarks in the hadron: the  $\Omega$  baryon ( $sss$ ) exhibits the largest enhancement, while the proton ( $uud$ ) sees virtually no increase. This provides even stronger evidence for the formation of a chemically equilibrated QGP, which no longer appears exclusive to heavy ion collisions.

While extensions to the aforementioned statistical models can describe these multiplicity-dependent particle ratios in a phenomenological manner **NATURE**17, the microscopic origins of this enhancement are not well understood. By investigating the production of strange hadrons in p–Pb collisions (where the onset is greatest), this thesis aims to shed light on the origins of this strange enhancement. However, it is necessary to first introduce some theoretical models to help interpret the results of

757 this thesis.

## 758 1.7 Heavy-Ion Collision Models

759 Theoretical models of heavy ion collisions are pertinent to the understanding of QCD  
760 and the QGP. Without them, there would be no framework for interpreting the results  
761 from the very expensive experiments dedicated to studying this strongly interacting  
762 plasma. Unfortunately, due to the complexity of these heavy ion collision systems,  
763 there is no *single* model that can describe the entire collision evolution. Instead, the  
764 choice of model to compare a particular observable to depends very heavily on the  
765 observable in question. For example, some models treat the QGP phase of the colli-  
766 sion as a hydrodynamic system, washing out information about the initial partonic  
767 scatterings **EPOS**. This can be useful when trying to study bulk properties of the  
768 QGP (like the  $v_2$  from Section ??), but not-so-useful when studying jets and their  
769 constituents. Other models focus more on the individual partonic scatterings and sub-  
770 sequent hadronization, but do not include an explicit QGP phase **Pythia**, **DPMJet**.  
771 Such models are powerful tools for analyzing smaller collision systems (pp and lower  
772 multiplicity p–Pb), but fail to capture many of the features observed in heavy ion  
773 collision data. In this section, the models used to help interpret the results of this  
774 thesis will be discussed. All of these models are capable of simulating pp, p–Pb, and  
775 Pb–Pb events.

### 776 1.7.1 PHSD

777 Parton-Hadron-String-Dynamics (PHSD) **PHSD1**, **PHSD2** is the only model ex-  
778 plored in this thesis that utilizes a **microscopic transport approach**: it simulates  
779 the full space-time evolution of a heavy-ion collision by modeling the interactions of  
780 individual particles. Here “particles” refers to different quantities (strings, partons,  
781 hadrons) which are all evolved in different ways. The transport equations of the  
782 partons and hadrons are derived from the Kadanoff-Baym (KB) equations **KBEq**,  
783 which describe the non-perturbative transport of particles in a strongly interacting  
784 system. The evolution of a collision within PHSD is as follows.

785 **1.7.1.1 Initial stages**

786 Prior to the collision, the simulation is broken up into a 3D-grid of size 56 in each  
 787 of the x, y, and z directions. The total size of the grid increases with each time step  
 788 such that the number of particles within a given cell evolves smoothly with time. The  
 789 initial momentum distribution and abundances of partons within the nuclei (prior to  
 790 any collision) are given by the thermal distributions

$$f(\omega, \vec{p}) = C_i p^2 \omega \rho_i(\omega, \vec{p}) n_{F/B}(\omega/\tau), \quad (1.21)$$

791 where  $\rho_i$  are the spectral functions of the quarks and gluons ( $i = q, \bar{q}, g$ ) and  $n_{F/B}$  are  
 792 the Fermi-Dirac (for quarks) and Bose-Einstein (for gluons) distributions. Once the  
 793 nuclei collide, the partons interact with each other under the Lund string model to  
 794 form *leading hadrons* (at large rapidity) and *pre-hadrons* (at midrapidity), as shown  
 795 in Figure ???. The leading hadrons are immune to dissociation within the QGP, while  
 796 the pre-hadrons are not.

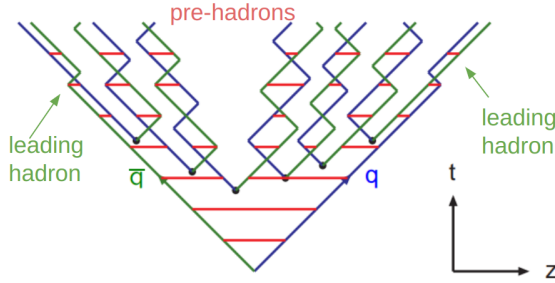


Figure 1.19: The Lund string model, with pre-hadrons and leading hadrons labeled.

797 **1.7.1.2 QGP phase**

798 If the energy density  $\epsilon$  of a given cell increases beyond the critical energy density  
 799  $\epsilon_c = 0.5 \text{ GeV/fm}^3$ , the pre-hadrons within that cell are dissolved into partons. The  
 800 partons are then treated as interacting quasi-particles under the DQPM **DQPM**  
 801 model, with Lorentzian spectral functions given by

$$\rho_j(\omega) = \frac{\gamma_j}{E_j} \left( \frac{1}{(\omega - E_j)^2 + \gamma_j^2} - \frac{1}{(\omega + E_j)^2 + \gamma_j^2} \right) \quad (1.22)$$

802 where  $i$  is one of  $(q, \bar{q}, g)$  and the width  $\gamma_i$  is given by

$$\gamma_g(T) = N_c \frac{g^2 T}{8\pi} \ln \frac{2c}{g^2}, \quad \gamma_q(T) = \frac{N_c^2 - 1}{2N_c} \frac{g^2 T}{8\pi} \ln \frac{2c}{g^2}, \quad (1.23)$$

803 where  $T$  is the temperature (calculated from the energy density within a given cell).  
804 This is the key difference between DQPM and other transport models—the quarks and  
805 gluons have non-zero temperature-dependent widths in the medium! The coupling  
806 constant  $g$  is also temperature dependent, and is of the form

$$g^2(T/T_c) = \frac{48\pi^2}{(11N_c - 2N_f) \ln(\lambda^2(T/T_c - T_s/T_c)^2)}. \quad (1.24)$$

807 The parameters  $T_s$  and  $\lambda$  are fit to lattice QCD (lQCD) results **PHSD2**. The spectral  
808 functions are enough to describe the propagation of the mean-fields of the partons  
809 (effectively their Greens functions) via the aforementioned KB equations. The col-  
810 lisional terms in these equations are determined by the modified scattering cross  
811 sections of the partons. These cross sections are calculated using the leading order  
812 Feynman diagrams, with the DQPM-modified quark and gluon propagators given by

$$i\delta_{ij} \frac{q + M_q}{q^2 - M_q^2 + 2i\gamma_q q_0} \quad (1.25)$$

813 and

$$-i\delta_{ab} \frac{g^{\mu\nu} - q^\mu q^\nu/M_g^2}{q^2 - M_g^2 + 2i\gamma_g q_0}, \quad (1.26)$$

814 respectively. Due to the large masses of the gluons,  $q + \bar{q} \rightarrow g + g$  and  $g \rightarrow g + g$  are  
815 suppressed and thus not included in the model.

### 816 1.7.1.3 Hadronization

817 Whenever the energy density of a given cell falls below the aforementioned critical  
818 energy density ( $\epsilon_c = 0.5$  GeV/fm $^3$ ), the partons within begin to hadronize. The  
819 dynamical hadronization of partons into hadrons is modeled by the equations

$$\begin{aligned} \frac{dN_m(x, p)}{d^4x d^4p} &= \text{Tr}_q \text{Tr}_{\bar{q}} \delta^4(p - p_q - p_{\bar{q}}) \delta^4\left(\frac{x_q + x_{\bar{q}}}{2} - x\right) \\ &\times \omega_q \rho_q(p_q) \omega_{\bar{q}} \rho_{\bar{q}}(p_{\bar{q}}) |v_{q\bar{q}}|^2 W_m(x_q - x_{\bar{q}}, (p_q - p_{\bar{q}})/2) \\ &\times N_q(x_q, p_q) N_{\bar{q}}(x_{\bar{q}}, p_{\bar{q}}) \delta(\text{flavor, color}). \end{aligned} \quad (1.27)$$

820 for mesons and

$$\frac{dN_B(x, p)}{d^4x d^4p} = \text{Tr}_{q_1} \text{Tr}_{q_2} \text{Tr}_{q_3} \delta^4(p - p_{\xi_3}) \delta^4(x - \xi_3) \delta\left(\sqrt{(\tau_1 - \tau_2)^2}\right)$$
$$\times \omega_{q_1} \rho_{q_1}(p_1) \omega_{q_2} \rho_{q_2}(p_2) \omega_{q_3} \rho_{q_3}(p_3)$$
$$\times |M_{qqq}|^2 W_B(\xi_1, \xi_2, p_{\xi_1}, p_{\xi_2})$$
$$\times N_{q_1}(x_1, p_1) N_{q_2}(x_2, p_2) N_{q_3}(x_3, p_3) \delta(\text{flavor, color}).$$
 (1.28)

821 for baryons. The terms for the meson case are described as follows:

- $\text{Tr}_q$  is shorthand notation for  $\text{Tr}_q = \sum_q \int d^4x_q \int \frac{d^4p_q}{(2\pi)^4}$ , where  $q$  is summed over all spin, color, and flavor degrees of freedom.
- $\delta^4(p - p_q - p_{\bar{q}})$  forces conservation of four-momentum. Note that the quarks and anti-quarks are allowed to be off-shell (due to their non-zero widths), thus this can result in off-shell mesons.
- $\delta^4\left(\frac{x_q + x_{\bar{q}}}{2} - x\right)$  puts the resulting meson in-between the quark and anti-quark pair.
- $\omega_q$  and  $\omega_{\bar{q}}$  are the energies of the quark and anti-quark, respectively.
- $\rho_q(p_q)$  and  $\rho_{\bar{q}}(p_{\bar{q}})$  are the aforementioned spectral functions of the quark and anti-quark, respectively.
- $|v_{q\bar{q}}|^2$  is the DQPM-determined *effective quark-anti-quark interaction*, which is shown as the green dashed line in Figure ???. Note that this value is very small for large quark (energy) densities, and thus this entire equation is effectively zero. However, for low quark densities this value blows up, which “turns on” the hadronization (and also guarantees that all partons will hadronize *eventually*).
- $W_m(x_q - x_{\bar{q}}, (p_q - p_{\bar{q}})/2)$  is the phase-space distribution of the resulting (pre-)meson
- $N_q(x_q, p_q)$  and  $N_{\bar{q}}(x_{\bar{q}}, p_{\bar{q}})$  are the phase-space densities of the quark and anti-quark, respectively.
- $\delta(\text{flavor, color})$  is shorthand for “make sure flavor quantum numbers are conserved and that the resulting meson is color-neutral”.

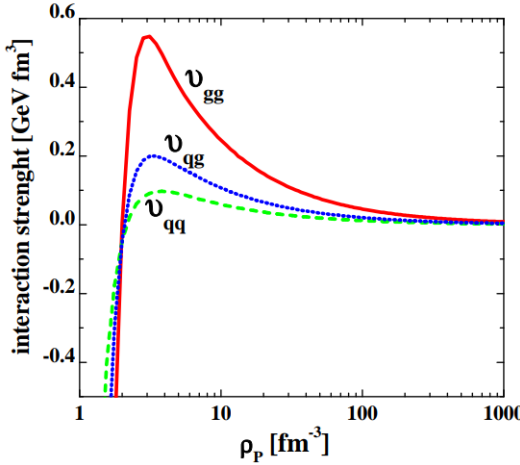


Figure 1.20: The effective quark-quark (green), quark-gluon (blue), and gluon-gluon (red) interactions as a function of parton density in DQPM, taken from **PHSD1**.

843 The terms for the baryon case are similar.

844 The numerical integrations of equations ?? and ?? for a fixed test parton ultim-  
 845 ately give the probability for a hadronization event to occur. From there, events  
 846 are randomly selected using Monte Carlo techniques, which give a color neutral state  
 847 with definite  $x$ ,  $p$  and flavor. However, this is *still* not enough to specify a hadron  
 848 completely: many hadronic states of the same flavor have large widths. Thus to  
 849 determine the identity of the final hadron, the weight of each possible<sup>24</sup> hadronic  
 850 spectral function is computed. The hadron is then randomly assigned an identity  
 851 based on these weights using Monte Carlo.

#### 852 1.7.1.4 Hadronic phase

853 All of the hadrons produced in the previous steps are transported using Hadron-  
 854 String-Dynamics **HSD** (PHSD without the P). The phase-space distributions of the

---

<sup>24</sup>PHSD only includes the baryon octet/decouplet, the spin 0 and spin 1 meson nonets, and a few higher resonance states. Furthermore, if the invariant mass of the color neutral state is above 1.3 GeV (for mesons) or 1.5 GeV (for baryons), the state is treated as a Lund string with further decay handled by the JETSET algorithm **JETSET**

hadrons in HSD are transported using the equation

$$\begin{aligned} & \left\{ \left( \Pi_\mu - \Pi_\nu \partial_\mu^p U_h^\nu - M_h^* \partial_\mu^p U_h^S \right) \partial_x^\mu + \left( \Pi_\nu \partial_\mu^x U_h^\nu + M_h^* \partial_\mu^x U_h^S \right) \partial_p^\mu \right\} f_h(x, p) \\ &= \sum_{h_2 h_3 h_4 \dots} \int d2d3d4 \dots [G^\dagger G]_{12 \rightarrow 34 \dots} \delta_\Gamma^4 (\Pi + \Pi_2 - \Pi_3 - \Pi_4 \dots) \\ & \quad \times \left\{ f_{h_3}(x, p_3) f_{h_4}(x, p_4) \bar{f}_h(x, p) \bar{f}_{h_2}(x, p_2) \right. \\ & \quad \left. - f_h(x, p) f_{h_2}(x, p_2) \bar{f}_{h_3}(x, p_3) \bar{f}_{h_4}(x, p_4) \right\} \dots, \end{aligned} \tag{1.29}$$

where  $U_h^S$  and  $U_h^\mu$  are the scalar and vector hadron self-energies, respectively. The effective mass of the hadron  $M_h^*$  is given by

$$M_h^* = M_h + U_h^S, \tag{1.30}$$

and its effective momentum is given by

$$\Pi^\mu = p^\mu - U_h^\mu. \tag{1.31}$$

The “collisional” term  $[G^\dagger G]_{12 \rightarrow 34 \dots}$  is the transition rate for the process  $1 + 2 \rightarrow 3 + 4 + \dots$ , which is modeled using Lund string fragmentation. The self-energies  $U_h^S$  and  $U_h^\mu$  are evaluated on the basis of a Nambu-Jona-Lasinio (NJL)-type model **NJL** for the QCD Lagrangian. Once these self-energies (and  $[G^\dagger G]_{12 \rightarrow 34 \dots}$ ) are specified, the transport equation (Equation ??) can be solved.

### 1.7.1.5 A simple overview

While the equations that govern PHSD are quite complicated, the overall picture is relatively simple. It can be summarized as follows:

- First, the simulation is split up into cells whose sizes evolve with time, as shown in Figure ??.
- As the initial nuclei collide, and the interacting partons form pre-hadrons and leading hadrons.
- If the energy density of a cell is too high, the pre-hadrons dissolve into partons, which are handled by the DQPM model.
- If a cell with partons in it cools off, the partons dynamically hadronize.
- The resulting hadrons (and any hadrons present in a particular cell) are transported using HSD.

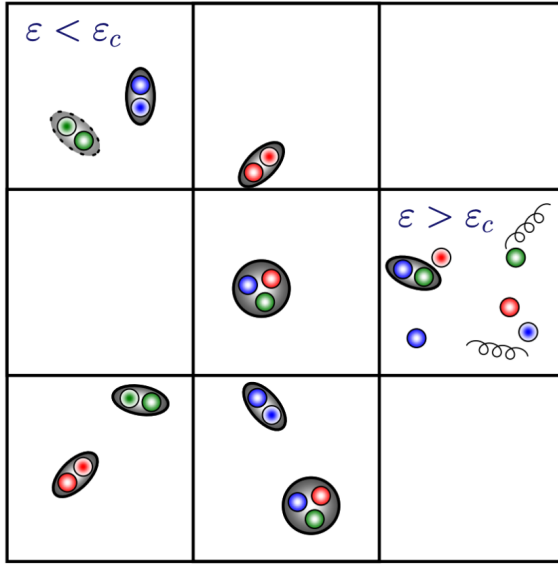


Figure 1.21: The cells within PHSD. If the energy density of the cell is greater than the critical energy density, the pre-hadrons dissolve into partons.

### 876 1.7.2 EPOS LHC

877 In the EPOS LHC **EPOS LHC** model, the initial colliding nuclei results in many  
 878 parton-parton scatterings happening in parallel, as shown in Figure ???. These si-  
 879 multaneous scatterings form a parton ladder, which are modeled as relativistic Lund  
 880 strings. Long before hadronization, the model separates into two distinct parts: the  
 881 *core* and the *corona*. This designation is based on the string density (i.e. the number  
 882 of string segments per unit volume). If the string density exceeds a critical density  
 883  $\rho_c$ , the string segments are considered to be in the core. Otherwise, they are in the  
 884 corona.

885 The core is evolved in a hydrodynamic manner, which loses all information about  
 886 the initial string segments and their interactions. Hadronization in the core is handled  
 887 by a microcanonical procedure known as Cooper-Frye freeze-out, which is described in  
 888 detail in **CooperFrye**. The core is associated with the QGP medium, and dominates  
 889 particle production at higher multiplicities. The corona, however, corresponds to  
 890 unmodified Lund string fragmentation, which dominates at large rapidity and in  
 891 lower multiplicity events.

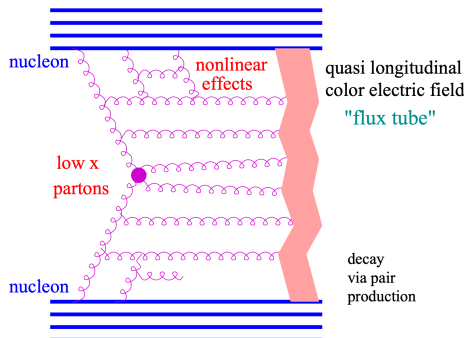


Figure 1.22: A schematic of the elementary interaction in EPOS LHC in which many parton-parton interactions are occurring simultaneously **EPOS LHC**.

### 892 1.7.3 DPMJET

893 Perhaps the most simple<sup>25</sup> event generator explored in this thesis is the DPMJET **DPMJET**  
 894 model. DPMJET combines the Dual Parton Model (DPM) **DPM** with the Lund  
 895 string model **LundString** to describe proton-proton, proton-nucleus, and nucleus-  
 896 nucleus collisions across a large range of energies. The DPM describes all of the soft,  
 897 non-perturbative multi-particle events that occur within a heavy ion collision using  
 898 various large  $N_c$  and  $N_f$  limits of QCD. This is the only model explored in this  
 899 thesis that does not have an explicit QGP phase, as the collision constituents<sup>26</sup> are  
 900 always treated independently. Thus DPMJET serves as a good baseline for vacuum  
 901 fragmentation, and can be compared with other models (and data) to help quantify  
 902 the effects of the explicit QGP phase.

---

<sup>25</sup>Still *extremely* complicated from a theoretical perspective, but has the least moving parts.

<sup>26</sup>Strings. It's always strings.

## Chapter Two: Summary and outlook

904 Quantum chromodynamics (QCD) is the theory that describes how the protons and  
905 neutrons, which compose almost all ordinary matter, are bound to one another within  
906 the nucleus of an atom. In this theory, the fundamental constituents of matter are  
907 *not* protons and neutrons, but rather quarks and gluons. These quarks and gluons  
908 bind together through their color charge, creating the color neutral hadrons observed  
909 in nature. One of the most interesting predictions of QCD is that, at extreme temper-  
910 atures and densities, these hadrons dissolve into their constituent quarks and gluons,  
911 forming a new state of matter known as the Quark-Gluon Plasma (QGP). Under-  
912 standing the QGP, which is thought to be the state of the universe shortly after the  
913 Big Bang, can help answer questions about the nature of everyday matter and the  
914 evolution of the universe.

915 Studying the QGP requires recreating the extreme conditions of the early uni-  
916 verse, which can only be achieved through high energy particle collisions. In such  
917 collisions, however, the QGP is only produced for a very short time, after which it  
918 expands and cools into the hadrons that are observed in the detector. Thus the QGP  
919 cannot be studied directly, and its formation and properties must be inferred from  
920 the information that is accessible to experiment. One of the first predicted exper-  
921 imental signatures for the formation of this plasma is the enhancement of strange  
922 hadron production, relative to non-strange pion production. While this enhancement  
923 was thought to be unique to heavy-ion collisions, experimental data from ALICE  
924 indicates that even high multiplicity pp and p–Pb collisions exhibit an onset of this  
925 enhanced production. This enhancement can only be described using statistical mod-  
926 els, as its microscopic origin is not yet understood.

927 One way to study the strange particles that are produced in these high energy  
928 collisions is through jets, which are sprays of hadrons that come from a hard inter-  
929 action of the partons inside the nuclei. By looking at how a high-momentum hadron  
930 (that represents a jet direction) and a lower momentum strange hadron are aligned  
931 in azimuthal angle, it is possible to separate the processes that create strangeness  
932 between hard (jet-related) and soft (QGP-related) ones. This angular correlation  
933 method can be used to further the understanding of how strangeness production de-

934 pends on the multiplicity in these different regimes, thus providing insight to the  
935 onset of strangeness enhancement in smaller collision systems.

936 This thesis presents the first results using angular correlations to measure jet and  
937 non-jet  $\Lambda$  and charged hadron production in p–Pb collisions at  $\sqrt{s_{\text{NN}}} = 5.02$  TeV. By  
938 using the technique of two-particle angular correlations, the production of  $\Lambda$  baryons  
939 can be separated into different kinematic regions: the near-side region (associated  
940 with jet-like strangeness production without QGP modification) away-side region  
941 (associated with jet-like production in the presence of the QGP), and the underlying  
942 event (tied to the uncorrelated strangeness production in the QGP). Both the yields  
943 and the jet widths on the near- and away-side regions are extracted from the azimuthal  
944 correlation functions and studied as a function of associated momentum and event  
945 multiplicity. A strong dependence on multiplicity is observed for both the near-  
946 and away-side yields in the case of the  $\Lambda$ , whereas the charged hadron associated  
947 yields exhibit a much smaller (nearly statistically insignificant) dependence. The  
948 away-side yields also show a systematically larger increase with multiplicity than the  
949 near-side yields for both cases, hinting at modification of the away-side production  
950 due to jet-QGP interactions. The h- $\Lambda$  and h-h near-side jet widths reveal a large  
951 dependence on  $p_{\text{T}}$ , becoming more collimated as momentum increases. The widths of  
952 the away-side jets are found to be independent of both  $p_{\text{T}}$  and multiplicity, however  
953 the larger systematic uncertainties introduce difficulties with excluding flat behavior.  
954 Comparing width values of the h- $\Lambda$  and h-h correlations, the h- $\Lambda$  near-side widths  
955 are found to be significantly ( $> 2\sigma$ ) larger than the dihadron widths, whereas the  
956 away-side widths are consistent within uncertainties. This indicates that  $\Lambda$  baryons  
957 are more readily produced in the peripheral regions of the jet cone, whereas charged  
958 hadrons are produced closer to the jet axis. This hints at a modification of the jet  
959 fragmentation process for strange hadrons, as more massive particles (like the  $\Lambda$ ) are  
960 expected to be produced closer to the jet axis.

961 The yield ratios  $R_i^{\Lambda/h}$  and  $R_i^{\Lambda/\phi}$  ( $i = \text{near-side jet, away-side jet, UE}$ ) are also  
962 studied as a function of associated  $p_{\text{T}}$  and multiplicity. The  $\Lambda/h$  ratios exhibit a clear  
963 ordering in each region for the entire multiplicity range in both  $p_{\text{T}}$  bins, with the  
964 UE ratios being larger than the away-side ratios, which are larger than the near-side  
965 ratios. This indicates that relative  $\Lambda$  production is larger in the UE (QGP) when  
966 compared to the jet-like regions. The  $\Lambda/h$  ratios in each region also reveal a strong  
967 dependence on multiplicity, with slopes that are greater than zero by nearly  $5\sigma$  for

968 both momentum bins. This indicates that while the overall  $\Lambda$  production is mostly  
969 concentrated in the UE, the observed enhancement of  $\Lambda$  production with increasing  
970 multiplicity is *also* driven by the jet-like regions. Furthermore, the away-side slopes  
971 are found to be systematically higher than the near-side slopes, indicating that the  
972 away-side  $\Lambda$  production is more strongly enhanced than the near-side  $\Lambda$  production  
973 with increasing multiplicity. Again, this suggests that the away-side jet strangeness  
974 production is modified by medium interactions. The  $\Lambda/\phi$  ratios in the near-side jet  
975 region are measured to be systematically higher than both the away-side and UE  
976 ratios, hinting at a suppression of  $\phi$  mesons along the jet axis due to the lack of  
977 available  $s$ -quarks in the unmodified jet. The slopes of these ratios in all kinematic  
978 regions are consistent with zero, indicating that the ratio is independent of collision  
979 centrality.

980 The measurements in this thesis are compared with theoretical predictions from  
981 the PHSD, EPOS and DPMJET models. PHSD is found to be in good agreement with  
982 all dihadron measurements, but fails to describe the overall  $\Lambda$  yields. This is likely  
983 due to the requirement of a high momentum trigger hadron, which are not readily  
984 produced within the model. Even still, the shape of the near-side peak in the h- $\Lambda$   
985 correlation distribution is well-described by PHSD. EPOS, on the otherhand, is able  
986 to describe the  $\Lambda$  and hadron yields very well, but the correlation distributions are  
987 dominated by elliptic flow, making it impossible to extract the jet-like components.  
988 This flow contribution is much larger for the h- $\Lambda$  distributions, indicating that  $\Lambda$   
989 baryons in EPOS are mostly produced within the hydronamic core. The predicted  
990 near- and away-side yields from DPMJET are found to be in relatively good agreement  
991 with data in the dihadron case, but the h- $\Lambda$  yield predictions deviate from data by a  
992 large ( $> 40\%$ ) margin. DPMJET also fails to predict any of the observed multiplicity  
993 dependence for both the h- $\Lambda$  and h-h jet yields. However, the model is able to closely  
994 predict the near-side widths of the dihadron distributions across all multiplicity and  
995 momentum ranges, although it underpredicts both the h- $\Lambda$  near-side widths and  
996 the away-side widths for both ( $\Lambda$ , h) cases. The model also predicts a difference  
997 between the h- $\Lambda$  and h-h near-side widths, which is observed in data as well. This  
998 indicates that whatever process responsible for the production of strangeness in the  
999 periphery of the jet cone is contained within DPMJET. The per-trigger  $\Lambda/h$  and  $\Lambda/\phi$   
1000 yield ratios are consistently underpredicted by DPMJET, and exhibit no multiplicity  
1001 dependence. Even still, DPMJET manages to predict the ordering of the  $\Lambda/h$  ratios

1002 in each region (UE > away-side jet > near-side jet) and the enhancement of the  
1003 jet-like  $\Lambda/\phi$  ratio when compared to the UE region. Thus the softer, uncorrelated  
1004 processes implemented in DPMJET are responsible for the majority of the relative  
1005 strangeness production.

1006 **2.1 Future outlook**

1007 The measurements presented in this thesis strongly indicate that, while the dom-  
1008 inating component for strangeness production comes from the QGP, the observed  
1009 *enhancement* of this production as a function of multiplicity has a large contribution  
1010 from the jet-like regions. More still, the away-side jet component appears to undergo  
1011 a larger enhancement than the near-side, hinting that the jet and medium are inter-  
1012 acting in such a way that strangeness is more readily produced. These observations  
1013 can be used to help fuel the theoretical models used to describe particle collisions, as  
1014 such models are currently incapable of describing these results in their entirety.

1015 The techniques presented in this thesis can be easily extended to other collision  
1016 systems, such as pp and Pb–Pb collisions, along with other particle species, such as  
1017 the  $K^0$ . With the advent of the Run 3 data-taking period at the LHC, the ALICE  
1018 detector will be able to collect more data than ever before, allowing for more precise  
1019 measurements of these observables across a wider range of particles and collision  
1020 systems. Such measurements will help further constrain the microscopic origins of  
1021 this strange enhancement, thus providing more insight into the nature of the QGP  
1022 and the universe as a whole.

1023

## Appendix A: Resonance technique for $\Lambda$ reconstruction

1024

1025

### A.1 Introduction

1026 This portion of the appendix is dedicated to describing the analysis procedure for  
 1027 generating the  $h-\Lambda$  correlation distributions using lambdas which are reconstructed  
 1028 using the **resonance technique**, where all proton-pion pairs in an event are com-  
 1029 bined to form  $\Lambda$  candidates. All of the proton and pion daughter tracks meet the  
 1030 same selection criteria as the tracks used in the  $V^0$  technique, described in Table ??.  
 1031 All in all, the procedure is very similar to the one described in Chapter ??, but with  
 1032 a few key differences that will be highlighted in the following sections.

1033

### A.2 Combinatorial background estimation

1034 As  $\Lambda$  baryons reconstructed using the resonance technique will have a much larger  
 1035 combinatorial background than those from the nominal procedure, the final correla-  
 1036 tion will contain a higher fraction of  $h-(p\pi)$  pairs that need to be removed. While  
 1037 the sideband subtraction technique provides a general procedure for removing these  
 1038 pairs, the signal  $S$  and the background  $B$  of the  $\Lambda$  invariant mass distribution must be  
 1039 well described. To estimate these quantities, the following techniques were explored:

1040

- **Like-sign  $p\pi$  pairs** - Reconstruct the invariant mass of like-sign (LS)  $p\pi$  pairs,  
 1041 and scale the like-sign  $p\pi$  distribution to the unlike-sign (US)  $p\pi$  distribution  
 1042 in a region outside of the  $\Lambda$  signal region.

1043

- **Rotated  $p\pi$  pairs** - Reconstruct the invariant mass of US  $p\pi$  pairs, but rotate  
 1044 either the pion or proton around the z-axis by  $\pi$  radians, and scale the rotated  
 1045  $p\pi$  distribution to the original US sign  $p\pi$  distribution in a region outside of  
 1046 the  $\Lambda$  signal region.

- 1047 • **Voigtian + polynomial fit** - Perform a standard fitting procedure using a  
 1048 Voigtian distribution for the signal along with a second-order polynomial for  
 1049 the background.

1050 The last technique will be addressed first, as it fails to properly estimate the signal  
 1051 and background in data. To illustrate this, the best possible fits in data are found  
 1052 and the corresponding signal shape is extracted and compared with the signal shape  
 1053 in Monte Carlo using full track reconstruction via GEANT. This comparison is done  
 1054 for the 20-50% multiplicity bin in Figure ???. Note that the background shown in the  
 1055 MC plot is the true combinatorial background, as the  $p\pi$  pairs are accessed directly  
 1056 at the generator level to confirm they did not come from a  $\Lambda$  decay.

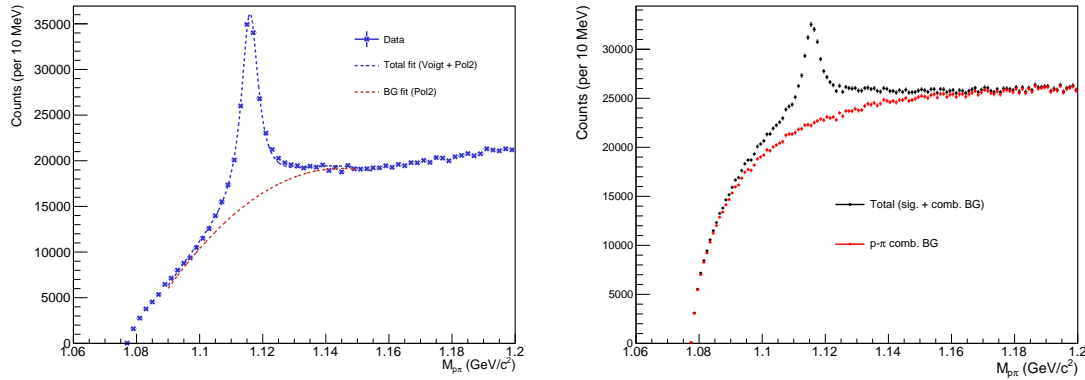


Figure A.1: Left: Invariant mass distribution with corresponding Voigt + Polynomial fit in the 20-50% multiplicity bin (data). Right: The signal and background shapes in MonteCarlo (MC). Note that even though MC appears to have a completely different S/B, the signal shapes should be similar. The fit in data appears to be massively underestimating the  $\Lambda$  signal, as the MC sample indicates there is  $\Lambda$  signal where the total data fit converges with the BG fit.

1057 This plot shows the main issue with reconstructing  $\Lambda$  baryons using the resonance  
 1058 technique: the tails of the signal distribution are much wider than the signal distri-  
 1059 bution obtained using the  $V^0$  method. This is due to the fact that the kinematics  
 1060 of the corresponding daughter tracks are calculated assuming they originated from  
 1061 the primary vertex, which is only approximately true in the cases where the  $\Lambda$  is  
 1062 short-lived. This is different than the  $V^0$  method, which calculates the kinematics for  
 1063 the daughter tracks assuming they originated from the secondary vertex. The wider  
 1064 tails of the distribution make it extremely difficult to describe using any common

1065 distribution, thus all techniques that rely on fitting the signal shape are not viable.  
 1066 Because of this, only the first two techniques (like-sign and rotated p $\pi$  pairs) will be  
 1067 considered for the rest of this analysis.

1068 To determine which of the two remaining techniques is more effective, the back-  
 1069 ground shape of the  $\Lambda$  invariant mass distribution for both techniques in MonteCarlo  
 1070 is compared to the ground-truth background shape. The resulting invariant mass  
 1071 distributions from like-sign and rotated p $\pi$  pairs are shown in Figure ??, along with  
 1072 a comparison of the extracted signal shapes. The LS and rotated p $\pi$  distributions are  
 1073 scaled to match the US distribution in the sideband region, which will be discussed  
 1074 in the next section. The LS p $\pi$  pairs match the background shape of the  $\Lambda$  invariant  
 1075 mass distribution more closely than the rotated p $\pi$  pairs, so they are used to estimate  
 1076 the combinatorial background in the  $\Lambda$  invariant mass distribution in data.

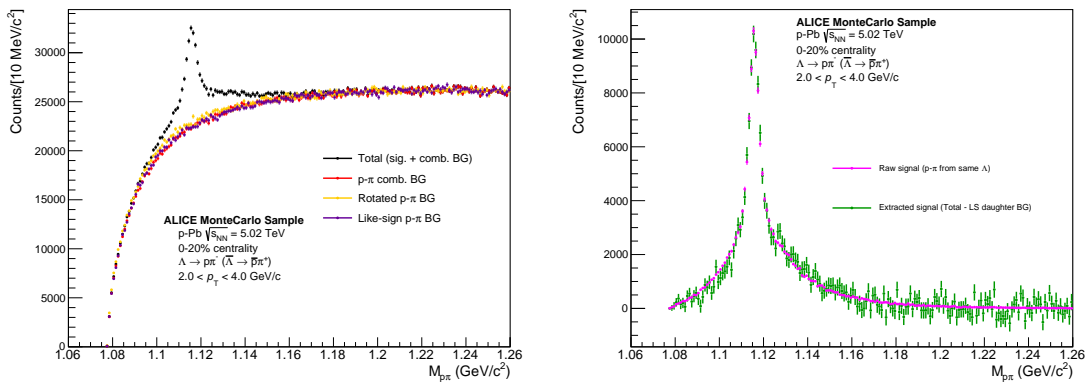


Figure A.2: Left: Invariant mass distribution for reconstructed unlike-sign p $\pi$  pairs (black) in the MonteCarlo sample. The like-sign p $\pi$  pair mass distribution (purple) and unlike-sign rotated p $\pi$  distributions are scaled to match the unlike-sign distribution outside of the  $\Lambda$  signal range. The true combinatorial background (red) matches most closely with the like-sign pairs. Right: The actual  $\Lambda$  signal (magenta) compared with the result of subtracting the like-sign from the total unlike-sign p $\pi$  distribution (green). The two distributions show good agreement.

### 1077 A.3 Signal and sideband regions

1078 As the invariant mass distributions from lambdas reconstructed using the resonance  
 1079 technique are very different from those reconstructed using the V<sup>0</sup> technique, so

too must the signal and sideband regions be different. The signal region was again chosen to maximize significance across all multiplicity bins, and is defined as the range  $1.014 < M_{p\pi} < 1.026 \text{ GeV}/c^2$ . Choosing the sideband region is a more complicated procedure, as there is no obvious region in the invariant mass distribution where the signal vanishes. Instead, the sideband region is chosen to minimize the difference between the extracted signal in data and the signal shape in MonteCarlo, which can be seen in Figure ???. The resulting sideband region is  $1.160 < M_{p\pi} < 1.180 \text{ GeV}/c^2$ .

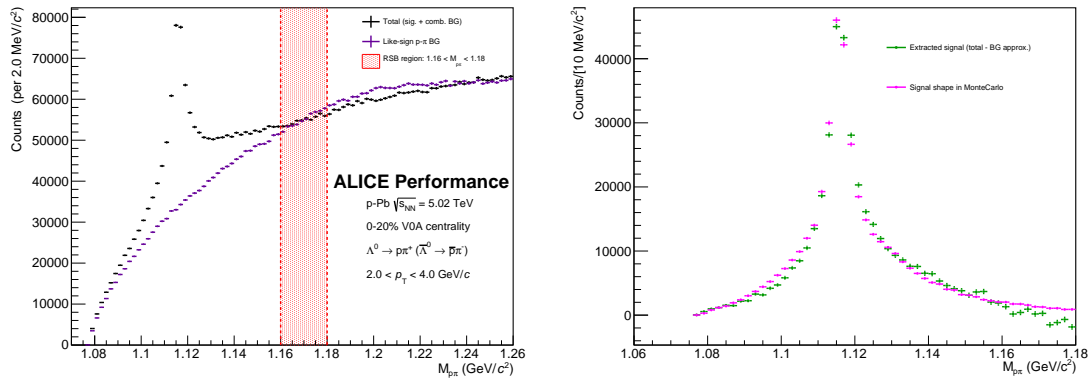


Figure A.3: Left: Invariant Mass distribution for unlike-sign  $p\pi$  pairs (black) along with the like-sign  $p\pi$  background (purple) and the sideband region (red) in the 0-20% multiplicity bin. Right: The extracted signal (green) compared with the resonance-technique reconstructed signal shape in MonteCarlo (magenta). The sideband region was chosen to minimize the differences between these distributions.

### 1087 A.3.1 Efficiency correction

1088 Again, the resonance technique-based  $\Lambda$  reconstruction efficiency is calculated in a  
1089 similar manner as the  $V^0$  technique, using the formula

$$\epsilon(x_1, x_2, \dots, x_n) = \frac{N_{\text{reco.}}(x_1, x_2, \dots, x_n)}{N_{\text{gen.}}(x_1, x_2, \dots, x_n)}, \quad (\text{A.1})$$

1090 where  $N_{\text{reco.}}$  and  $N_{\text{gen.}}$  are the reconstructed and generated particle distributions with  
1091 kinematic variables  $x_1, x_2, \dots, x_n$ . The main difference from the  $V^0$  efficiency computa-  
1092 tion comes from  $N_{\text{reco.}}$ , where each  $\Lambda$  candidate is generated using the following  
1093 procedure:

- 1094 • Find all protons and pions within the track list that pass the daughter selection  
1095 criteria

- 1096     • For each proton in the list, determine if it came from a  $\Lambda$  (at generator level)
- 1097     • If the proton came from a  $\Lambda$ , loop through the pion list until the pion that came  
1098       from the same  $\Lambda$  is found (again, verified at the generator level)
- 1099     • Reconstruct the  $\Lambda$  using the daughter tracks found in the previous two steps
- 1100     • Only keep the  $\Lambda$  if  $|\eta| < 0.8$
- 1101     The denominator  $N_{\text{gen.}}$  is calculated in the same way as the  $V^0$  technique. The  
1102     resulting efficiency is shown as a function of  $p_T$  for each multiplicity bin in Figure ??.
- 1103     As expected, the efficiency is higher than the  $V^0$  technique, as every  $\Lambda$  reconstructed  
1104     using the resonance technique would also be reconstructed using the  $V^0$  technique.

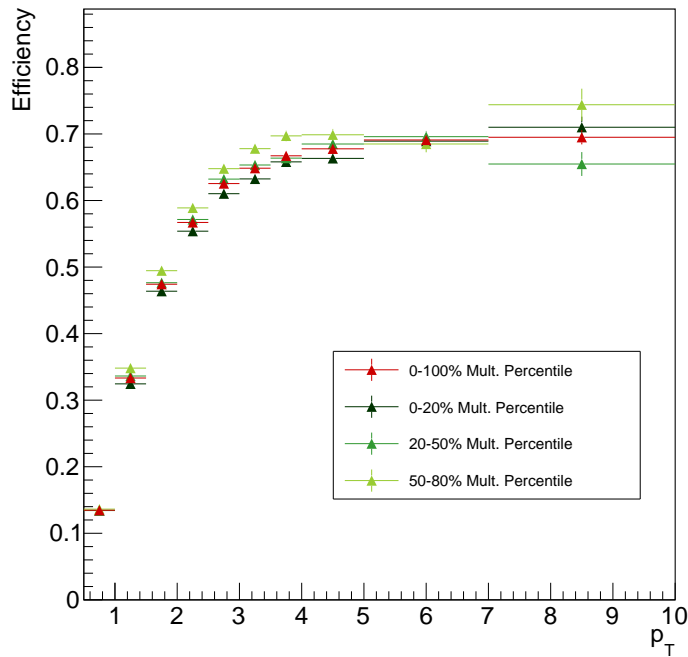


Figure A.4: Efficiency vs.  $p_T$  for  $\Lambda$  reconstruction using resonance technique for each multiplicity bin, along with an integrated 0-100% point in red. There does not appear to be any significant dependence on multiplicity. Also worth nothing that the efficiency is higher for this technique when compared to the  $V^0$  technique, as expected (all AOD tracks from  $V^0$  finder daughters are also in total AOD track list).

## 1105 A.4 Corrections to the h- $\Lambda$ distributions

1106 All of the efficiency and acceptance corrections are applied to the resonance technique-based h- $\Lambda$  distribution in the same way as the V<sup>0</sup> technique. The only difference comes  
 1107 from the removal of the combinatorial background, as:

- 1109 1. The signal  $S$  and background  $B$  are calculated in a slightly different manner,  
 1110 and
- 1111 2. The sideband region is vastly different.

1112 For the first point, the signal and background are calculated via bin-wise summation  
 1113 of the invariant mass distribution using the LS p $\pi$  pairs as an estimate for the  
 1114 background, scaled to the US distribution in the sideband region.

1115 The second point is mostly inconsequential as the h-p $\pi$  distributions are very  
 1116 similar in a wide range of sideband regions, as shown in Figure ???. The nominal  
 1117 sideband region was chosen to be  $1.160 < M_{\text{SSB}} < 1.180 \text{ GeV}/c^2$ , but any region with  
 1118 a lower bound greater than  $1.160 \text{ GeV}/c^2$  and upper bound less than  $1.22 \text{ GeV}/c^2$   
 1119 should produce similar results.

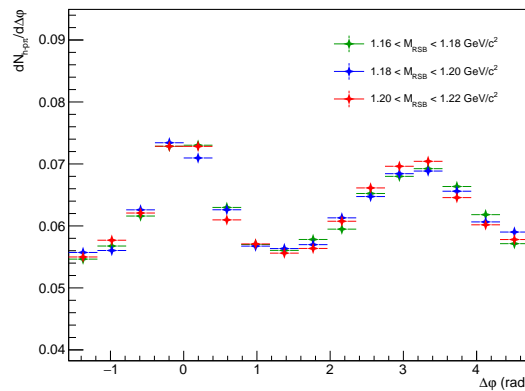


Figure A.5: The projected  $\Delta\varphi$  distributions for different choices of sideband, taken within the  $-1.2 < \Delta\eta < 1.2$  region. The correlation shapes are identical within the statistical errors.

1120 The signal scaling factor is calculated in the same way as it is in Equation ??, but  
 1121 with the residual now generated by subtracting the sideband-scaled LS p $\pi$  pairs from  
 1122 the US distribution. The two-track efficiency correction is not applied, as the tools

1123 used to calculate the  $\epsilon_{\text{pair}}(\Delta\varphi, \Delta\eta)$  template were not developed before the resonance  
 1124 technique-based analysis was completed.

## 1125 A.5 MC closure test

1126 An MC closure test was also performed for the resonance technique-based analysis,  
 1127 and the results are shown in Figure ???. The ratio is consistent with unity, but the  
 1128 statistical fluctuations make it difficult to draw any meaningful conclusions.

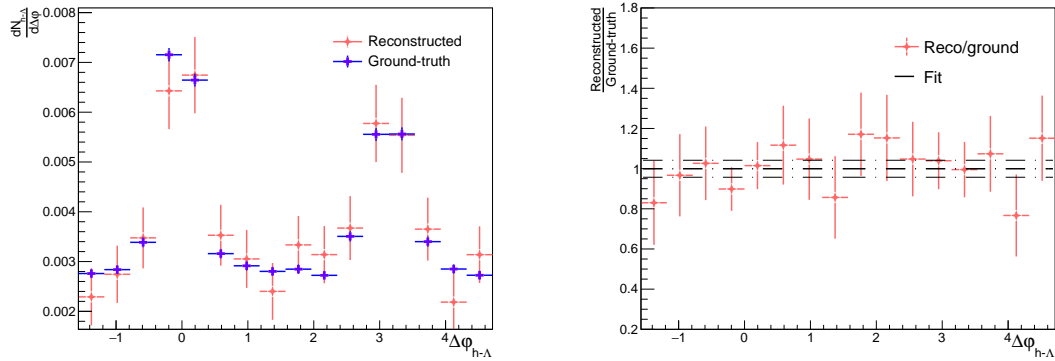


Figure A.6: The reconstructed (red) and ground-truth (blue)  $h\text{-}\Lambda_{\text{res}}$   $\Delta\varphi$  distributions along with a (reconstructed)/(ground-truth) ratio and straight-line fit. The fit is technically consistent with unity, but the statistical fluctuations are quite large.

1129 As the reconstructed distribution has not been corrected for the two-track merging  
 1130 effect, it is surprising that the ratio does not exhibit a significant deviation from unity  
 1131 at small  $\Delta\varphi$ . This is likely due to two factors:

- 1132 1. The resonance technique has a much lower S/B, and therefore the sideband  
 1133 subtraction introduces a large amount of statistical fluctuations making such  
 1134 deviations difficult to observe, and
- 1135 2. The reconstructed daughter tracks have a larger fraction of higher quality tracks  
 1136 when compared to the  $V^0$  technique, and those tracks are less likely to be merged  
 1137 over by the trigger during reconstruction.

1138 To elaborate on the second point, while the resonance and  $V^0$  techniques use the  
 1139 same loose quality cuts, the daughter tracks coming from the  $V^0$  technique must

1140 have a resolvable secondary vertex, which biases the corresponding  $\Lambda$  sample to those  
 1141 with a higher decay length. As discussed in ??, the two-track merging effect is  
 1142 more pronounced at larger decay lengths, thus the  $h\text{-}\Lambda$  distributions using the  $V^0$   
 1143 reconstruction technique will have a larger fraction of merged tracks when compared  
 1144 to the resonance technique-based distributions.

1145 To further investigate this surprising closure of the resonance technique-based  $h\text{-}\Lambda$   
 1146  $\Delta\varphi$  distributions, the same closure test is performed, but for the reconstructed  $h\text{-}\Lambda$   
 1147 distribution, the  $\Lambda$  candidate is required to have have a corresponding particle at the  
 1148 generator-level, making the combinatorial background exactly zero and removing the  
 1149 need for sideband subtraction. The results of this test are shown in Figure ???. The  
 1150 ratio is no longer consistent with unity at small  $\Delta\varphi$ , as expected<sup>1</sup>

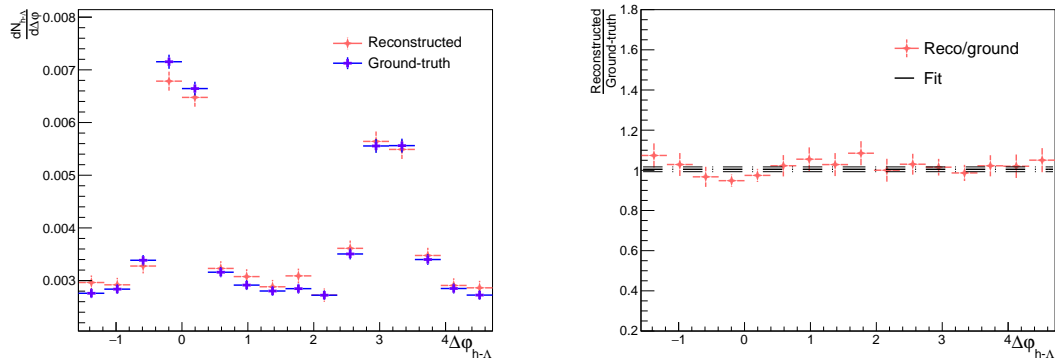


Figure A.7: The reconstructed (red) and ground-truth (blue)  $h\text{-}\Lambda_{\text{res}}$   $\Delta\varphi$  distributions along with a (reconstructed)/(ground-truth) ratio and straight-line fit, but instead requiring the reconstructed  $\Lambda$  to have a corresponding particle at the generator level to make sideband subtraction unnecessary. The result is no longer consistent with unity at small  $\Delta\varphi$  due to the track merging effect, but the non-closure is much smaller than the  $V^0$  technique.

## 1151 A.6 Some additional results

1152 A comparison of the final per-trigger  $h\text{-}\Lambda$   $\Delta\varphi$  correlation structure from the resonance  
 1153 and  $V^0$ -based techniques was shown in Chapter ??, but it can be seen again in

---

<sup>1</sup>It is strange to *want* non-closure, but it would be even stranger if the track merging effect were somehow not present in the resonance technique-based analysis.

1154 Figure ???. As mentioned previously, the correlation shapes are nearly identical, with  
 1155 the resonance technique having slightly larger uncertainties due to the combinatorial  
 1156 background subtraction.

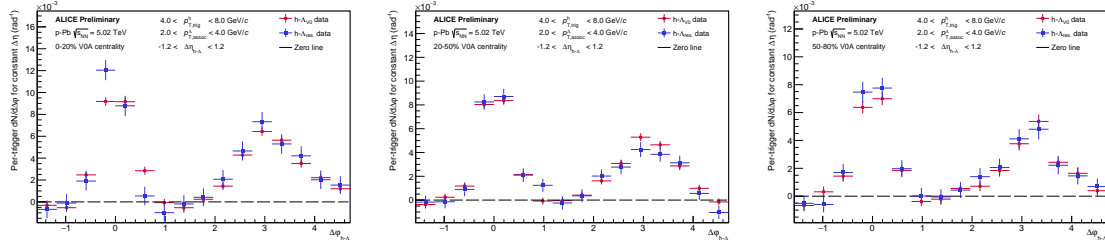


Figure A.8: The final per-trigger  $h\text{-}\Lambda$   $\Delta\varphi$  correlations for  $\Lambda$ s reconstructed using the resonance technique (blue) and the  $V^0$ -based technique (red) in the 0-20% (left), 20-50% (middle) and 50-80% (right) multiplicity bins, taken in the associated momentum range  $2.0 < p_T < 4.0 \text{ GeV}/c$ , after the subtraction of the UE. The distributions show good agreement across all multiplicity bins, indicating that the  $V^0$ -based reconstruction technique is not introducing a bias in the correlation shape.

1157 Additionally, the per-trigger near- and away-side pairwise yields and the  $(h\text{-}\Lambda)/(h\text{-}h)$   
 1158 ratios with  $\Lambda$ s reconstructed using the resonance technique are shown in Figure ???.  
 1159 The results are qualitatively very similar to the nominal results, indicating that the  
 1160 resonance technique is a reasonably viable alternative to the  $V^0$  technique. How-  
 1161 ever, due to the larger combinatorial background (and likely very large systematic  
 1162 uncertainties), the  $V^0$  technique is still the preferred method for  $\Lambda$  reconstruction.

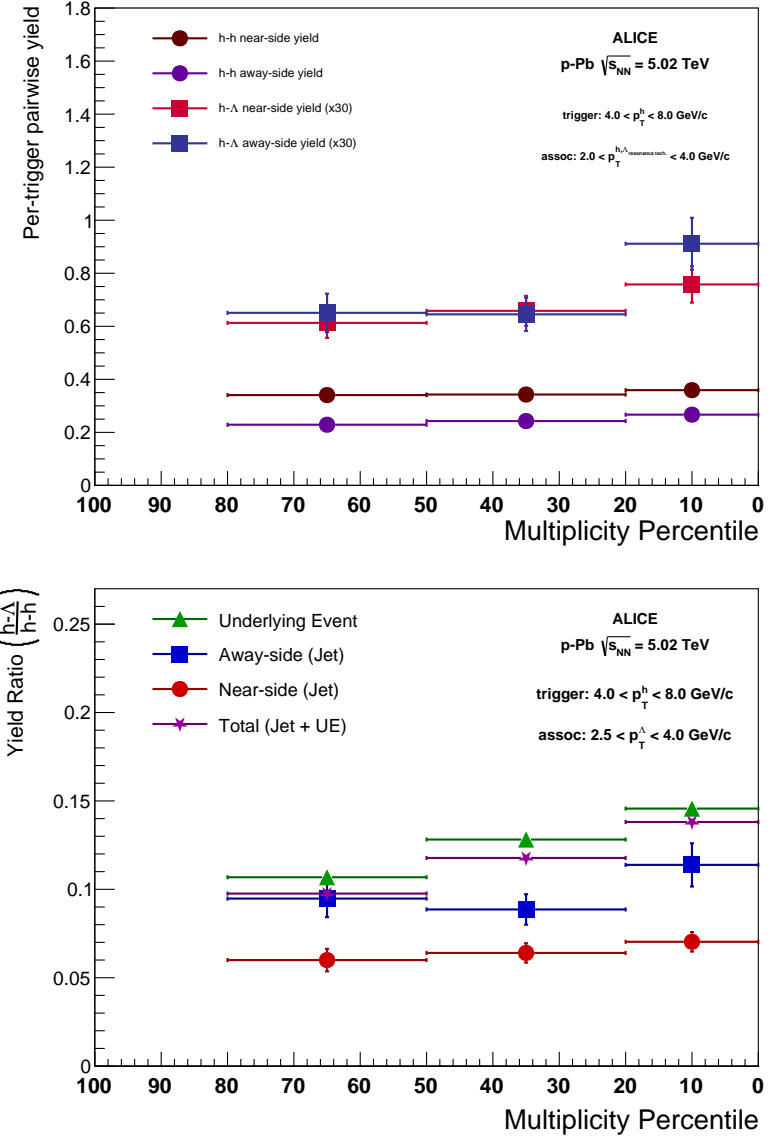


Figure A.9: The final  $h\text{-}\Lambda$  and  $h\text{-}h$  per-trigger pairwise jet yields (top) and  $(h\text{-}\Lambda)/(h\text{-}h)$  yield ratios (bottom) vs. multiplicity in the associated momentum range  $2.0 < p_T < 4.0 \text{ GeV}/c$  for  $\Lambda$ s reconstructed using the resonance technique. The general trends are similar to the nominal  $V^0$  technique-based procedure, with larger statistical uncertainties.